SO and SiS emission tracing an embedded planet and compact 12CO and 13CO counterparts in the HD 169142 disk

Law, C.J.; Booth, A.S.; Öberg, K.I.

The Astrophysical Journal Letters, 952:L19 (19pp), 2023 July 20 https://doi.org/10.3847/2041-8213/acdfd0

SO and SiS Emission Tracing an Embedded Planet and Compact ^{12}CO and ^{13}CO Counterparts in the HD 169142 Disk

Charles J. Law[1], Alice S. Booth[2], and Karin I. Öberg[1]
[1] Center for Astrophysics | Harvard & Smithsonian, 60 Garden St., Cambridge, MA 02138, USA; charlesjlaw1@gmail.com
[2] Leiden Observatory, Leiden University, 2300 RA Leiden, The Netherlands
Received 2023 March 14; revised 2023 May 30; accepted 2023 June 20; published 2023 August 2

Abstract

Planets form in dusty, gas-rich disks around young stars, while at the same time, the planet formation process alters the physical and chemical structure of the disk itself. Embedded planets will locally heat the disk and sublimate volatile-rich ices, or in extreme cases, result in shocks that sputter heavy atoms such as Si from dust grains. This should cause chemical asymmetries detectable in molecular gas observations. Using high-angular-resolution ALMA archival data of the HD 169142 disk, we identify compact SO $J = 8_8 - 7_7$ and SiS $J = 19 - 18$ emission coincident with the position of a $\sim 2\,M_{\rm Jup}$ planet seen as a localized, Keplerian NIR feature within a gas-depleted, annular dust gap at ≈38 au. The SiS emission is located along an azimuthal arc and has a morphology similar to that of a known ^{12}CO kinematic excess. This is the first tentative detection of SiS emission in a protoplanetary disk and suggests that the planet is driving sufficiently strong shocks to produce gas-phase SiS. We also report the discovery of compact ^{12}CO and ^{13}CO $J = 3 - 2$ emission coincident with the planet location. Taken together, a planet-driven outflow provides the best explanation for the properties of the observed chemical asymmetries. We also resolve a bright, azimuthally asymmetric SO ring at ≈24 au. While most of this SO emission originates from ice sublimation, its asymmetric distribution implies azimuthal temperature variations driven by a misaligned inner disk or planet–disk interactions. Overall, the HD 169142 disk shows several distinct chemical signatures related to giant planet formation and presents a powerful template for future searches of planet-related chemical asymmetries in protoplanetary disks.

Unified Astronomy Thesaurus concepts: Astrochemistry (75); Protoplanetary disks (1300); Planet formation (1241); Planet–disk interactions (2204); High angular resolution (2167)

1. Introduction

Planets form and inherit their compositions in dusty, gas-rich disks around young stars, while the planet formation process is expected to simultaneously alter the physical and chemical structure of the disk. Observations of protoplanetary disks using the Atacama Large Millimeter/submillimeter Array (ALMA) have revealed the presence of ubiquitous rings and gaps in the millimeter dust distribution (ALMA Partnership et al. 2015; Andrews et al. 2018; Huang et al. 2018; Cieza et al. 2021) and in molecular line emission (Bergner et al. 2019; van Terwisga et al. 2019; Facchini et al. 2021; Law et al. 2021; Öberg et al. 2021). In some cases, the millimeter continuum and molecular line emission appear azimuthally asymmetric (Tang et al. 2012; Booth et al. 2021a, 2023; van der Marel et al. 2021a, 2021b). While such features broadly suggest the presence of embedded planets, it remains difficult to unambiguously connect individual substructures seen in dust and line emission with the location and properties of nascent planets.

Nonetheless, a variety of methods for identifying and characterizing embedded planets in disks have been developed. Planet formation is thought to occur within dust gaps, and the properties of the observed dust distributions have been used to infer planet characteristics (e.g., Kanagawa et al. 2015; Zhang et al. 2018), while in a few systems, circumplanetary disks (CPDs) are detected via their excess millimeter continuum emission (Keppler et al. 2018; Benisty et al. 2021; Wu et al. 2022). However, such detections remain relatively scarce (Isella et al. 2014; Pineda et al. 2019; Andrews et al. 2021), which may be due to mm dust depletion and high gas-to-dust ratios (>1000) in CPDs (Karlin et al. 2023). Thus, the identification of planetary signals in molecular gas provides a promising complementary approach. While planetary signatures are now often indirectly seen via kinematic perturbations in the rotation velocity profiles of bright lines (e.g., Teague et al. 2018; Pinte et al. 2020), the first CPD candidate in molecular gas was discovered in ^{13}CO gas in the AS 209 disk (Bae et al. 2022). A similar planetary counterpart was recently identified in ^{12}CO gas in the Elias 2–24 disk (Pinte et al. 2023).

Embedded planets are also expected to directly alter the chemical structure of disks. In particular, forming-planets should locally heat the disk (e.g., Szulágyi 2017; Szulágyi et al. 2018), which will sublimate volatile-rich ice, or in more extreme cases, drive shocks that sputter heavy atoms such as Si from dust grains. This will result in chemical asymmetries that can be detected in sensitive line emission observations (Cleeves et al. 2015; Rab et al. 2019). Sufficiently deep observations of molecular gas with ALMA have only recently become available to enable searches for such chemical signatures. For instance, asymmetric SO line emission was found to trace an embedded planet in the HD 100546 disk (Booth et al. 2023), and Alarcón et al. (2022) identified a signature in CI gas potentially attributable to either the inflow or outflow associated with a protoplanet in the HD 163296 disk.

In this Letter, we present high-angular-resolution ALMA archival observations of the HD 169142 disk. We identify several chemical signatures related to ongoing planet formation,

including spatially localized SO and SiS emission and the discovery of compact ^{12}CO and ^{13}CO emission counterparts, which are all approximately coincident with an embedded giant planet. In addition, spatially resolved SO emission has only been detected in a handful of Class II disks to date (Pacheco-Vázquez et al. 2016; Booth et al. 2018, 2021a, 2023; Huang et al. 2023), and we report the first tentative detection of SiS in a protoplanetary disk. In Section 2, we describe the HD 169142 disk. We present the ALMA observations in Section 3. We present our results in Section 4, and discuss the chemical origins of the observed emission and possible connections with nascent planets within the HD 169142 disk in Section 5. We summarize our conclusions in Section 6.

2. The HD 169142 Disk and Evidence for Embedded Planets

HD 169142 is a Herbig Ae star (Blondel & Djie 2006) located at a distance of $d = 115$ pc (Bailer-Jones et al. 2021; Gaia Collaboration et al. 2021) and has a dynamically estimated stellar mass of $M_* = 1.4\,M_*$ (Yu et al. 2021), luminosity of $L_* = 10\,L_\odot$ (Fedele et al. 2017), and age of $\sim$ 10 Myr (Pohl et al. 2017). The disk surrounding HD 169142 has a nearly face-on orientation with an inclination of $i = 13°$ and position angle of PA $=5°$ (Raman et al. 2006; Panić et al. 2008).

The HD 169142 disk consists of several ring-like structures observed across many wavelengths, including in NIR/scattered light (e.g., Quanz et al. 2013; Reggiani et al. 2014; Pohl et al. 2017; Bertrang et al. 2018; Ligi et al. 2018; Gratton et al. 2019), thermal mid-infrared (Honda et al. 2012), (sub)mm (e.g., Fedele et al. 2017; Macías et al. 2019; Pérez et al. 2019), and cm (Osorio et al. 2014). Many of these structures have been posited to originate from planet–disk interactions. While varying numbers and masses of planets have been suggested, most studies require at least one $\gtrsim M_{\rm Jup}$ planet to explain the observed disk substructures. For a detailed summary of the proposed locations and types of embedded planets, the interested reader may see Yu et al. (2021), Garg et al. (2022), and references therein. Here, we restrict our focus to the annular gap located at an approximate radius of 41 au ("D41") in-between two major rings at $\approx$25 au ("B25") and $\approx$60 au ("B60"). The D41 gap is observed in both mm continuum and NIR/scattered light.

Multiple lines of evidence point to a planetary origin of the D41 gap, including hydrodynamic simulations (Bertrang et al. 2018; Toci et al. 2020), a decreased gas surface density (Fedele et al. 2017; Garg et al. 2022), and a localized kinematic excess in ^{12}CO within this gap (Garg et al. 2022). The most direct evidence of an embedded planet is in the form of NIR observations, which revealed a localized emission feature within this annular gap that is in Keplerian rotation around the central star, as well as the presence of a spiral-like structure consistent with a planet-driven wake (Gratton et al. 2019; Hammond et al. 2023). This feature was suggested to correspond to a $\sim 2\,M_{\rm Jup}$ still-accreting planet at a radius of $\approx$38 au (Gratton et al. 2019). Taken together, these may indicate that the planet is responsible for carving this gas-depleted, annular gap; exciting a spiral wake in the NIR; and triggering the observed ^{12}CO kinematic excess. Overall, this makes the HD 169142 disk an ideal source to search for chemical signatures associated with an embedded giant planet.

3. Observations

3.1. Archival Data and Observational Details

We made use of ALMA archival projects 2012.1.00799.S (PI: M. Honda) and 2015.1.00806.S (PI: J. Pineda), which we hereafter refer to as P2012 and P2015, respectively. P2012 comprises three execution blocks with baselines ranging from 15 to 1574 m, and P2015 has a single execution block with baselines of 19–7716 m. Appendix A provides detailed information about each project.

Both projects had two narrow spectral windows (244.1 kHz; $\approx$0.12 km s^{-1}) centered on the ^{12}CO $J = 3-2$ and ^{13}CO $J = 3-2$ lines. In addition, P2012 had two spectral windows covering the frequency ranges of 331.055–332.93 GHz and 343.055–344.929 GHz but at a coarse velocity resolution (976.6 kHz; $\approx$0.45 km s^{-1}). P2015 instead included one spectral window from 342.555 to 344.429 GHz but at an even coarser velocity resolution (1128.9 kHz; $\approx$0.85 km s^{-1}) and a dedicated continuum window. Within these spectral windows, we imaged the following lines: ^{12}CO $J = 3-2$, ^{13}CO $J = 3-2$, SO $J = 8_8-7_7$, SO_2 $J = 4_{3,1}-3_{2,2}$, SO_2 $J = 11_{6,6}-12_{5,7}$, and SiS $J = 19-18$. Table 1 lists details for each image cube.

The CO and SO lines are included in spectral setups in both P2012 and P2015. For the CO lines, we use both projects because each had dedicated spectral windows with high velocity resolution. For SO, we initially imaged the line using both the P2012-only and P2012+P2015 data and confirmed it is robustly detected in both combinations. However, due to the considerably coarser channel spacing of the P2015 data ($\approx$0.85 km s^{-1}), we performed all subsequent analysis of SO using only the P2012 data. The SiS and SO_2 lines are only covered in P2012. We generated the 0.9 mm continuum image using data from both projects and used the full bandwidth of the observations after flagging the channels containing line emission. Table 1 lists which project was used to generate each image cube.

Transitions of additional S- and Si-bearing molecules of interest (e.g., SiO, CCS, OCS, and NS) were not included in the spectral setup of either project.

3.2. Self-calibration and Imaging

Each archival project was initially calibrated by ALMA staff using the ALMA calibration pipeline and the required version of CASA (McMullin et al. 2007), before switching to CASA `v5.4.0` for self-calibration. Self-calibration was attempted on the shorter baseline data from P2012 alone, but we were unable to derive solutions that improved image quality. Data from both projects were combined and one round of phase self-calibration was applied, following the same procedure described in Öberg et al. (2021). We subtracted the continuum using the `uvcontsub` task with a first-order polynomial.

We then switched to CASA `v6.3.0` for all imaging. We used the `tclean` task to produce images of all transitions with Briggs weighting and Keplerian masks generated with the `keplerian_mask` (Teague 2020) code. Each mask was based on the stellar and disk parameters of HD 169142 and was visually inspected to ensure that it contained all emission present in the channel maps. Due to the non-Keplerian nature of the SiS emission, no masking was used to generate the SiS images. Briggs `robust` parameters were chosen manually to prioritize line detections with high signal-to-noise ratios (S/Ns). Channel spacings ranged from 0.12 to 0.44 km s^{-1},

Table 1
Image Cube and Line Properties

Transition	Freq. (GHz)	Beam ($''\times''$, deg)	JvM ϵ[a]	robust	Chan. δv (km s^{-1})	rms (mJy beam^{-1})	Project Used	E_u (K)	A_{ul} ($\log_{10}$ s^{-1})	g_u	Int. Flux[b] (mJy km s^{-1})
0.9 mm cont.	331.000000	0.05 × 0.03, 79.6	0.42	−0.5	…	0.1	P2012+P2015	…	…	…	420 ± 10
^{12}CO $J = 3-2$	345.795990	0.11 × 0.09, 74.2	0.64	0.5	0.12	3.9	P2012+P2015	33	−5.603	7	27,958 ± 228
^{13}CO $J = 3-2$	330.587965	0.14 × 0.11, 75.1	0.67	0.5	0.12	3.1	P2012+P2015	32	−5.960	14	10,664 ± 205
SO $J = 8_8 - 7_7$	344.310612	0.19 × 0.14, 84.4	…	2.0	0.43	1.5	P2012	88	−3.285	17	120 ± 16
SO_2 $J = 4_{3,1}-3_{2,2}$	332.505242	0.20 × 0.15, 88.2	…	2.0	0.44	1.4	P2012	31	−3.483	9	<32
SO_2 $J = 11_{6,6}-12_{5,7}$	331.580244	0.20 × 0.15, 88.2	…	2.0	0.44	1.5	P2012	149	−4.362	23	<43
SiS $J = 19 - 18$	344.779481	0.19 × 0.14, 84.3	…	2.0	0.43	1.6	P2012	166	−3.155	39	62 ± 23

Notes. The spectroscopic constants for all lines are taken from the CDMS database (Müller et al. 2001, 2005; Endres et al. 2016).

[a] The ratio of the CLEAN beam and dirty beam effective area used to scale image residuals to account for the effects of non-Gaussian beams. See Section 3.2 as well as Jorsater & van Moorsel (1995) and Czekala et al. (2021) for further details.

[b] Uncertainties are derived via bootstrapping and do not include the systematic calibration flux uncertainty (∼10%). The 3σ upper limits are reported for nondetections. The continuum flux has units of mJy.

depending on the line. All images were made using the multiscale deconvolver with pixel scales of [0,5,15,25] and were CLEANed down to a 4σ level, where σ was the rms measured in a line-free channel of the dirty image. Table 1 summarizes all image properties.

For the ^{12}CO, ^{13}CO, and continuum images, we applied the "JvM" correction proposed in Jorsater & van Moorsel (1995) and described in more detail in Czekala et al. (2021). This correction scales the image residuals by a factor ϵ, equal to the ratio of the effective areas of the CLEAN beam and dirty beam, to be in units consistent with the CLEAN model. Table 1 lists all ϵ values.

3.3. Moment Maps, Radial Profiles, and Integrated Fluxes

We generated velocity-integrated intensity, or "zeroth-moment," maps of line emission from the image cubes using `bettermoments` (Teague & Foreman-Mackey 2018) and closely followed the procedures outlined in Law et al. (2021). No flux threshold for pixel inclusion, i.e., sigma clipping, was used, to ensure accurate flux recovery. All maps were generated using the same Keplerian masks employed during CLEANing, except in the case of SiS, where we used hand-drawn masks to better capture the non-Keplerian emission (see Appendix C). `bettermoments` also provides a map of the statistical uncertainty that takes into account the nonuniform rms across the zeroth-moment map, which is described in detail in Teague (2019a). We take the median rms from these uncertainty maps as the zeroth-moment map uncertainty. We also generated peak intensity maps using the quadratic method of `bettermoments`.

We computed radial line intensity profiles using the `radial_profile` function in the `GoFish` python package (Teague 2019b) to deproject the zeroth-moment maps. All radial profiles assume a flat emitting surface. We computed the integrated fluxes for all lines with the same masks used to generate the zeroth-moment maps. We estimated uncertainties as the standard deviation of the integrated fluxes within 500 randomly generated masks at the same spatial position, but spanning only line-free channels. We report 3σ upper limits for the two undetected SO_2 lines. Table 1 lists all integrated fluxes.

4. Results

4.1. Spatial Distribution of Emission

4.1.1. CO Emission Morphology

Figure 1 shows zeroth-moment maps of the detected lines. The ^{12}CO and ^{13}CO $J = 3 - 2$ lines are the most spatially extended and display two emission rings, closely resembling the $J = 2 - 1$ transitions presented in Yu et al. (2021) and Garg et al. (2022) and the ^{13}CO $J = 6 - 5$ line from Leemker et al. (2022). In this Letter, we do not analyze the large-scale CO emission in detail, and instead we refer the interested reader to the above references.

4.1.2. SO Emission Morphology

Figure 2 shows an azimuthally averaged SO radial profile. The bulk of the SO emission is located in an azimuthally asymmetric ring at a radius of ≈24 au, which closely traces the inner mm dust ring (Figure 1). This SO ring exhibits a clear asymmetry, with the southern half of the disk showing bright SO emission while the northern half has only faint emission. Given the current data quality, it is difficult to precisely determine the degree of azimuthal asymmetry, but the peak brightness likely varies by at least a factor of several. A fainter outer ring at ≈50 au is also detected, which is clearly seen in the radial profile (Figure 2) and is visible as diffuse emission in the zeroth-moment map (Figure 1). Due its low S/N, we cannot assess if this outer SO ring is also asymmetric. There also appears to be a central dip in SO intensity at ≈11 au, but the true depth of this feature is difficult to quantify.

In addition to this ring-like morphology, SO shows a point-source-like emission feature at a radius of 32 au and PA ≈35°. This feature is not spatially resolved, and its compact nature is most clearly visible in the peak intensity map (Figure 1) and in the channel maps (in Appendix C). We also confirm that this feature is robustly detected in images with a range of Briggs `robust` parameters (see Appendix B). We often colloquially refer to such localized features as emission "blobs" and designate them by cardinal directions, i.e., "SO NE Blob." In Figure 2, we also extracted a radial profile along a narrow azimuthal wedge containing this feature. The SO NE Blob is not part of either SO ring, due its distinct radius, and the PA of this feature corresponds to the azimuthal region of the inner SO ring that shows little-to-no emission.

4.1.3. SiS Detection and Emission Morphology

We report the first tentative detection of SiS in a protoplanetary disk. SiS emission is detected with a peak intensity of 7.9 mJy beam^{-1}, which corresponds to a peak S/N of 5σ (Figure 1). We also detected peak SiS emission of at least 4σ in three velocity channels, two of which are consecutive (see Appendix C). Despite passing traditional thresholds for line detections (e.g., Bergner et al. 2019), we conservatively refer to this as a tentative detection because only one SiS line is covered in these archival data.

The SiS emission is spatially compact, azimuthally asymmetric, and non-Keplerian. As shown in Figure 2, the SiS emission can be broadly categorized into two distinct components: (1) a localized emission feature ("SiS NE Blob") at a position similar, but not identical, ($r \approx 40$ au; PA = 30°) to that of the compact SO feature; and (2) an extended arc or "tail" connected that extends to $r \approx 50$ au. These features can also clearly be seen in the channel maps in Appendix C. Similar to the SO feature, the SiS NE Blob is spatially unresolved, but due to its extended nature, the SiS tail is marginally resolved.

4.2. Kinematics of SO and SiS

In Figure 3, we first extracted disk-integrated spectra for SO and SiS, as well as for ^{13}CO, to provide a reference for the Keplerian rotation of the disk. The SO emission is consistent with Keplerian rotation and has a double-peaked profile similar to that of ^{13}CO. However, there is conspicuous excess flux at $v_{\rm LSR} \approx 8$ km s^{-1}, which represents the contribution of the bright NE Blob. While the SO NE Blob does not substantially deviate from Keplerian rotation, it has no bright localized counterpart on the other side of the disk, i.e., $v_{\rm LSR} < v_{\rm sys}$. In contrast to SO, the SiS emission is entirely non-Keplerian, with most emission coming from a narrow velocity range of $v_{\rm LSR} \approx 1$–2.5 km s^{-1}, while some fainter emission is present at $v_{\rm LSR} > 2.5$ km s^{-1}. This deviation from Keplerian rotation is clearly see in the channel maps (Appendix C). The hand-drawn SiS masks are intentionally restrictive, and the mask edges at

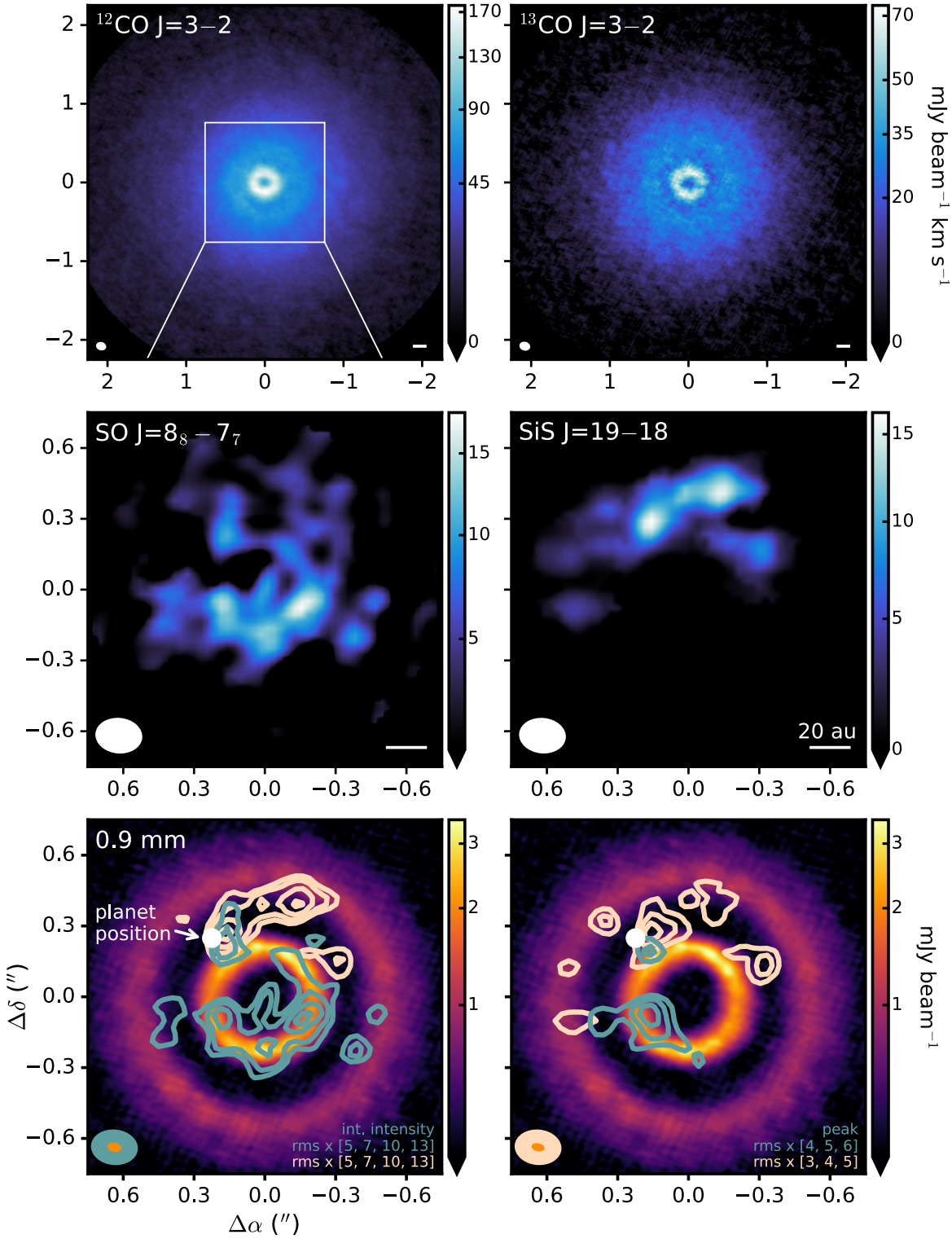

Figure 1. Top two rows: zeroth-moment maps of ^{12}CO $J = 3 - 2$, ^{13}CO $J = 3 - 2$, SO $J = 8_8 - 7_7$, SiS $J = 19 - 18$ for the HD 169142 disk. The synthesized beam and a scale bar indicating 20 au are shown in the lower left and right corner, respectively, of each panel. Bottom row: composite image of the 0.9 mm continuum emission (colorscale) with contours showing the integrated (left) and peak intensity (right) of SO and SiS. The rms for the integrated intensities represents the zeroth-moment map uncertainty. For the peak intensities, the rms is the channel map noise. The planet location from Gratton et al. (2019) and Hammond et al. (2023) is marked by a white circle. The synthesized beams for the continuum (orange), SO (teal), and SiS (peach) are shown in the lower left corners. The disk rotation is clockwise.

$v_{\rm LSR} = 7.1\,{\rm km\,s^{-1}}$ are shown in Figure 3. While the true SiS integrated flux may be larger than what is reported in Table 1, we opted for this conservative approach to ensure high confidence in the SiS emission we consider.

Next, we extracted individual spectra within one beam size at the location of the bright NE Blob in SO and SiS. The extraction positions are not identical, given the small spatial offset (a few au) between the SO and SiS features (Figure 1).

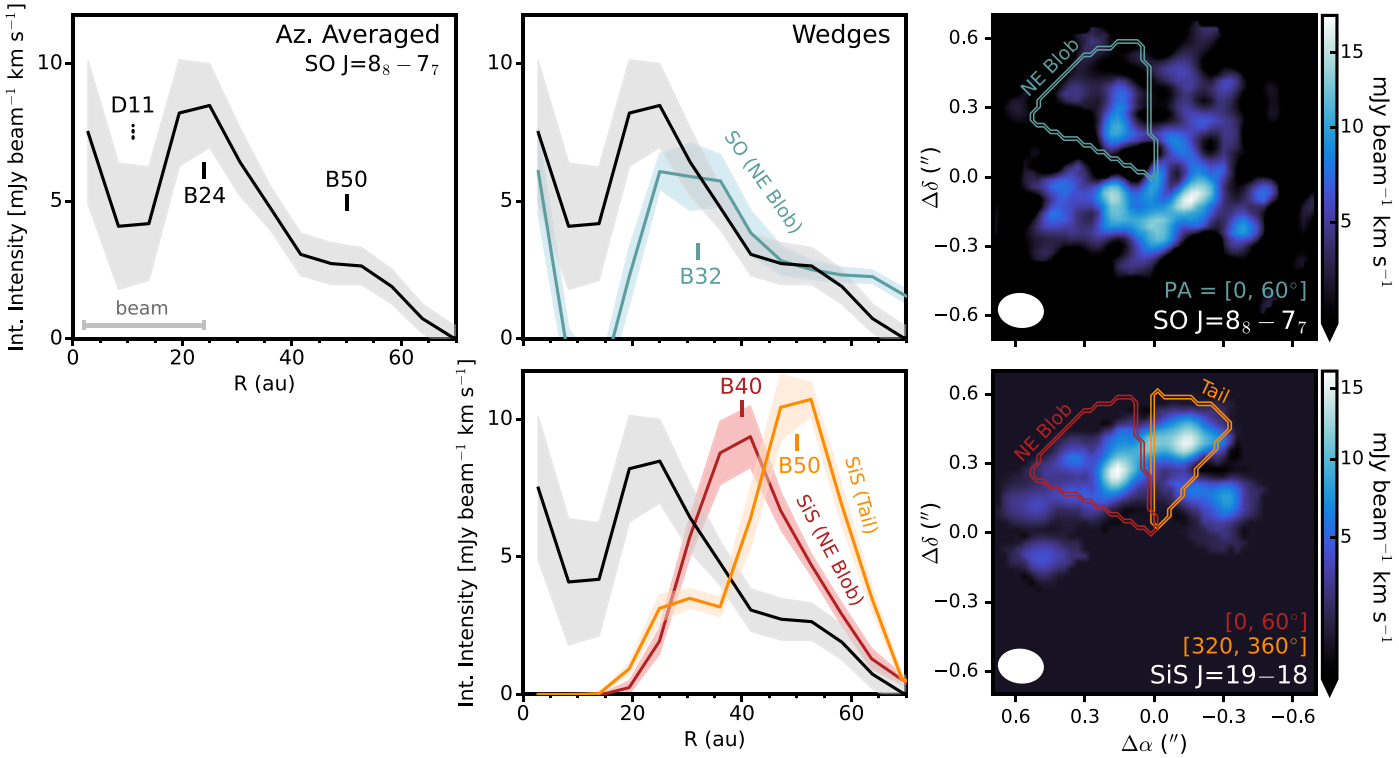

Figure 2. Deprojected radial intensity profiles of SO and SiS for the HD 169142 disk (left, middle columns). Shaded regions show the 1σ uncertainty. Solid lines mark rings and dotted lines denote gaps. The major axis of the synthesized beam is shown in the lower left corner. SO and SiS emission profiles are extracted from narrow wedges over the labeled PA range, measured east of north in the sky frame. These wedges are illustrated in the associated zeroth-moment maps (right column).

As before, we also extracted a ^{13}CO spectrum at the same position for reference. The SO emission associated with the SO NE Blob is consistent with the Keplerian rotation of the disk, while the SiS emission shows a blueshift of 6 km s^{-1} from the expected Keplerian velocity as traced by ^{13}CO. This SiS shift may point to a outflow around an embedded planet, and we return to this in the Discussion. Intriguingly, we also note the presence of excess, non-Keplerian ^{13}CO emission at a velocity ($v_{\rm LSR} \approx 5$ km s^{-1}) similar to that of the SiS emission.

More detailed analysis of the velocity structure of these lines is precluded by the relatively coarse channel spacing (≈0.4 km s^{-1}) of the ALMA archival data.

4.3. Point-source-like Emission in ^{12}CO and ^{13}CO

As shown in Figure 4, we also detected point-source-like emission in ^{12}CO and ^{13}CO at a projected distance of 340–400 mas (39–46 au) and PA ≈ 38°, which is near the location of the SO and SiS NE Blobs and the planet location. This emission is not related to the Keplerian component of the disk, and no counterpart to either feature in ^{12}CO or ^{13}CO is seen on the other side of the disk (e.g., see the full spectrum of ^{13}CO in Figure 3). We detected 3σ emission in at least two adjacent channels for both ^{12}CO and ^{13}CO (Figure 4). We confirmed that these features are robustly detected in both the JvM and non-JvM-corrected images, as well as in images generated from various combinations of `robust` parameters (see Appendix B for full details).

The ^{12}CO and ^{13}CO emission do not share the same velocity, with the ^{12}CO emission being more blueshifted ($v_{\rm LSR} \approx 3$ km s^{-1}) than the ^{13}CO component ($v_{\rm LSR} \approx 5$ km s^{-1}). While the ^{12}CO and ^{13}CO emission are approximately spatially coincident, the ^{12}CO emission appears slightly offset from the peak of ^{13}CO. The compact ^{13}CO is spatially unresolved, while there is a slight hint that ^{12}CO has a brighter northern component (see Appendix D), with the caveat that the entire extent of the ^{12}CO emission is within one beam. To better quantify this offset, we measured the centroids of the ^{12}CO and ^{13}CO emission in each channel with a full listing of the centroid locations in Appendix D.

No counterpart in millimeter continuum emission is detected here or reported in previous high-sensitivity continuum observations of this disk (e.g., Pérez et al. 2019). NIR colors of a point-source-like object suggest the presence of a significant amount of small dust at this location (Hammond et al. 2023). This is consistent with the presence of a Jupiter-mass planet, as the lack of mm dust can be explained by strong dust filtration (Rice et al. 2006), while the smaller dust grains remain coupled to the gas close to the protoplanet.

4.4. Column Densities

Next, we used the measured line intensities of SO, SiS, and SO_2 to compute their column densities (for a detailed analysis of the CO gas density, see Garg et al. 2022 and Leemker et al. 2022). We followed a similar analysis as in Booth et al. (2023) and assumed that the lines are optically thin and in local thermodynamic equilibrium (LTE). For SO and SiS, we only have one transition (and thus one upper state energy) and were unable to drive a rotational temperature ($T_{\rm rot}$). Likewise, for SO_2, both lines are undetected, which precludes a meaningful rotational diagram analysis. Instead, we adopted a constant rotational temperature of 100 K for all molecules. This is a reasonable assumption as all SO and SiS emission is confined to the inner disk (<70 au) and is consistent with the warm gas temperatures reported in Leemker et al. (2022).

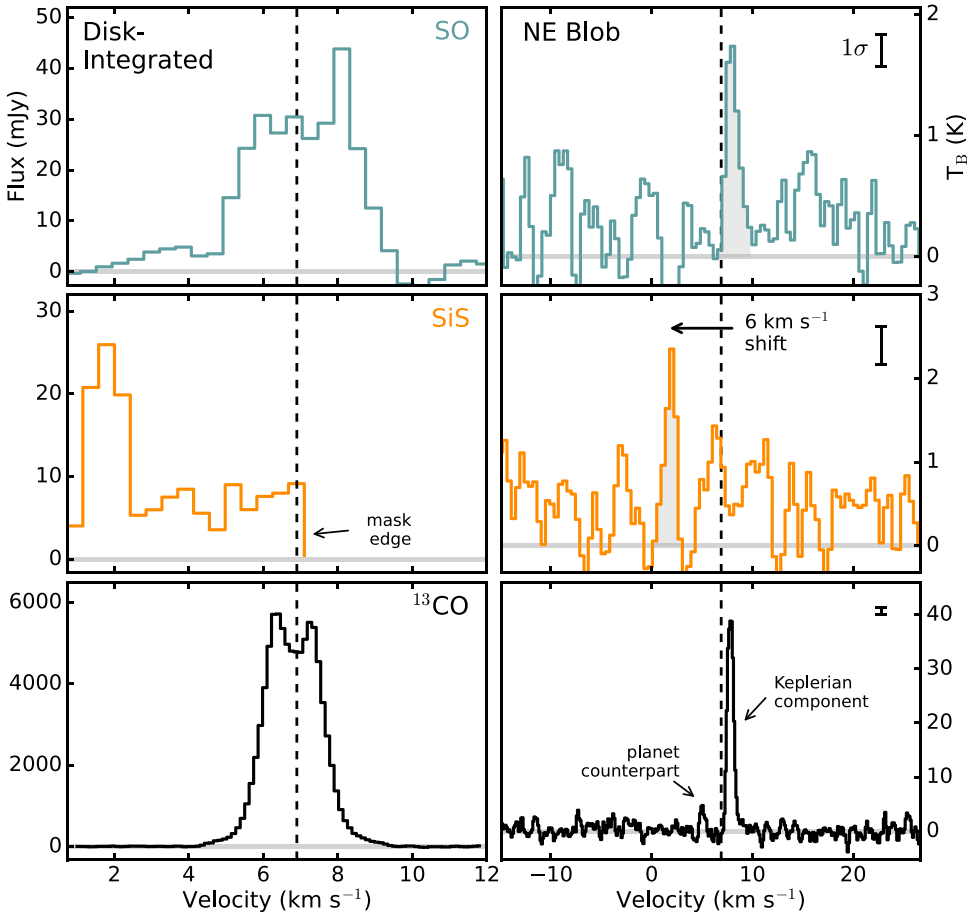

Figure 3. Disk-integrated spectra (left) and the spectrum at the position of the NE Blob extracted from a single beam (right) for SO, SiS, and ^{13}CO. The vertical dashed line indicates the systemic velocity of 6.9 km s^{-1}. For the individual spectrum, the rms is computed as the standard deviation of line-free channels and is shown in the upper right of each panel. The shaded regions in the SO and SiS spectra show the velocity regions used to compute the column densities in Table 2. A non-Keplerian, compact emission counterpart to the planet location is labeled in the ^{13}CO spectrum.

Figure 5 shows the SO radial column density profile computed using the azimuthally averaged radial line intensity profile (Figure 2). Disk-averaged column densities for SO, SiS, and SO_2 were estimated from the integrated fluxes and upper limits reported in Table 1 and an assumed elliptical emitting area with the same position angle and inclination as the disk and a semimajor axis of 0.″6. Table 2 lists the derived values.

We also derived the column densities at the location of the NE Blob. We used the fluxes of SO and SiS (and 3σ upper limit for SO_2) from spectra extracted within a single beam centered on the NE Blob position (Figure 3). The SO column density is a factor of two larger than the disk-averaged values, while the SiS column density is approximately an order of magnitude larger, resulting in a nearly one-to-one SiS/SO ratio at this position.

It is possible that the gas temperatures at the NE Blob are considerably higher than 100 K, especially because SiS is observed in the gas phase, which suggests the presence of shocks and dust grain sputtering. We note that the column density calculations are only modestly sensitive to the assumed temperature, i.e., if the temperature were a factor of five larger, this would result in an increase by a factor of two in SiS column density. Additional lines of SO and SiS with a sufficiently large range of upper state energies are required to better constrain the excitation conditions of both molecules.

5. Discussion

In Section 5.1, we discuss the nature and origins of the compact emission observed in multiple molecular tracers in the context of ongoing giant planet formation in the HD 169142 disk. In Section 5.2, we then explore the chemical origins of the broader ring-like SO emission, including the prominent asymmetry of the inner SO ring, and compare our observations to other Class II disks.

5.1. Chemical Signatures of Ongoing Giant Planet Formation

5.1.1. Compact ^{12}CO and ^{13}CO Emission Counterparts

The compact ^{12}CO and ^{13}CO emission is located at the center of a gas-depleted, mm and NIR annular gap (e.g., Fedele et al. 2017; Ligi et al. 2018; Pérez et al. 2019; Garg et al. 2022), is coincident with the position of a high-intensity, Keplerian-rotating NIR point source (Gratton et al. 2019; Hammond et al. 2023), and lies along the same azimuthal arc as a known ^{12}CO kinematic excess (Garg et al. 2022). Figure 6 shows the close proximity of this compact emission with the location of the HD 169142 b planet from Gratton et al. (2019) and Hammond et al. (2023). These different lines of evidence suggest that we are observing molecular line emission associated with a giant planet embedded within the HD 169142 disk. This represents the third such feature seen in molecular gas, after those

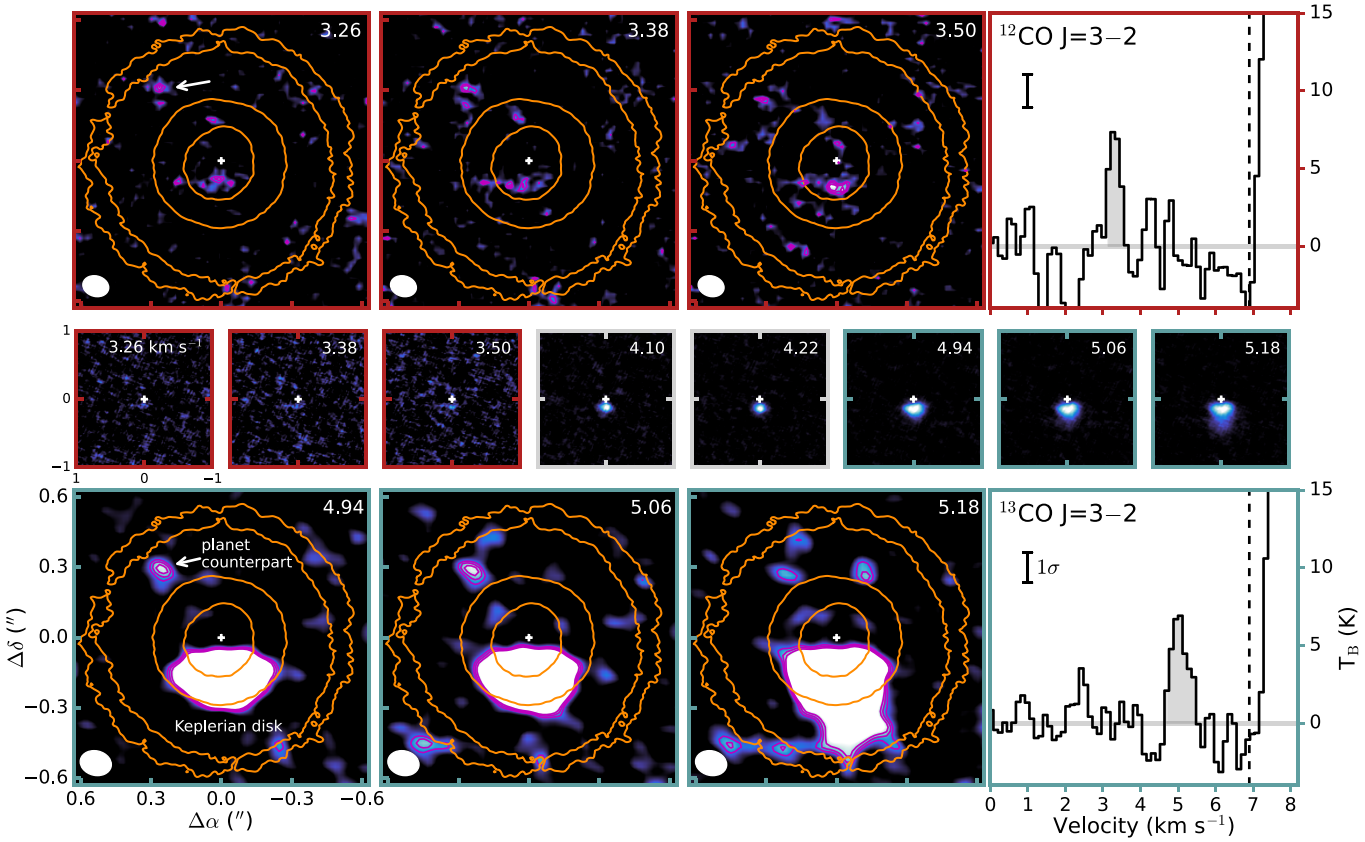

Figure 4. Selected channel maps and spectra extracted from a single beam at the position of the point-source-like emission in ^{12}CO $J = 3 - 2$ (upper row; red border) and ^{13}CO $J = 3 - 2$ (lower row; blue border). The middle row shows the ^{12}CO channels for reference, with the border color corresponding to each set of channels. Several channels (gray border) between 3.50 and 4.94 km s^{-1} have been omitted for the sake of visual clarity. The orange contours show the millimeter dust rings. The colorscale shows the line emission and has been intentionally saturated to highlight the faint emission associated with a point source at a projected distance of 340–400 mas and PA ≈ 38°. Contours in pink show rms × [2.5, 3, 3.5]. The synthesized beam is shown in the lower left corner of each panel. We show the JvM-uncorrected images here to provide the most conservative estimate of the S/N of the compact ^{12}CO and ^{13}CO emission. A comprehensive analysis of both JvM- and non-JvM-corrected images is provided in Appendix B.

identified in the AS 209 (Bae et al. 2022) and Elias 2–24 disks (Pinte et al. 2023), and the first seen in more than one molecular line.

With the current data, we cannot definitively determine the origin of this compact ^{12}CO and ^{13}CO emission. However, the significant blueshifts of both lines with respect to the systemic velocity suggest that this emission is not directly associated with a CPD or nearby circumplanetary material (Perez et al. 2015). Instead, the observed velocities are more consistent with an outflow origin, where we are observing gas accelerating along our line of sight, while the velocity difference between the more blueshifted ^{12}CO emission versus that of ^{13}CO is likely an optical depth effect. The tentative spatial offset of ^{12}CO from the more point-source-like emission of ^{13}CO is also consistent with such a scenario.

Further detailed analysis is limited by the current S/N. Data with higher angular and spectral resolution are required in order to better constrain the origin and properties of this compact ^{12}CO and ^{13}CO emission.

5.1.2. Localized SO and Arc-like SiS Emission

We first discuss the potential chemical origins of SO and SiS, which are generally considered tracers of shocked gas, and then interpret the observed chemical signatures in the HD 169142 disk in the context of giant planet formation. Here, we only consider the compact SO that is cospatial with the planet location; Section 5.2 provides a discussion of the bulk SO emission.

Table 2
Derived Column Densities

Molecule	N_{col} (cm^{-2})	/ SO (%)
Disk-averaged		
SO	$2.1 \pm 0.3 \times 10^{13}$	…
SiS	$6.5 \pm 2.4 \times 10^{12}$	31
SO_2	$<4.2\times10^{13}$	< 199
NE Blob		
SO	$4.9 \pm 0.7 \times 10^{13}$	…
SiS	$4.5 \pm 0.7 \times 10^{13}$	92
SO_2	$<4.3\times10^{13}$	<87

Notes. All column densities are computed assuming a constant $T_{ex} = 100$ K. For the two nondetected SO_2 lines, we computed the upper limit as 3σ for both lines and report the smaller of the two.

SO. SO is often observed in regions of warm and shocked gas, including accretion shocks (Sakai et al. 2014, 2017; Oya et al. 2019), protostellar outflows (Codella et al. 2014; Taquet et al. 2020), MHD-driven disk winds (Tabone et al. 2017; Lee et al. 2018), and the warm inner envelopes of Class I protostars (Harsono et al. 2021). In shocks, the gas temperature rapidly

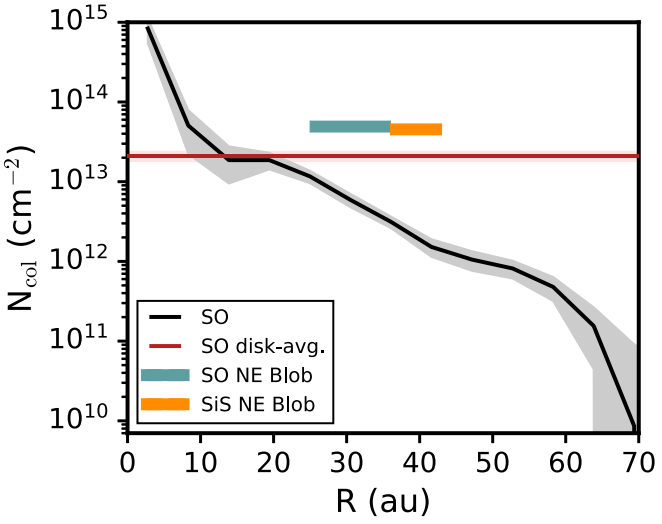

Figure 5. Radial column densities of SO and SiS derived with a constant $T_{rot} = 100$ K. The SO radially resolved profile is shown in black, and the disk-averaged SO value is marked by a horizontal red line. The column densities of the NE Blob for SO and SiS are shown as teal and orange rectangles, respectively.

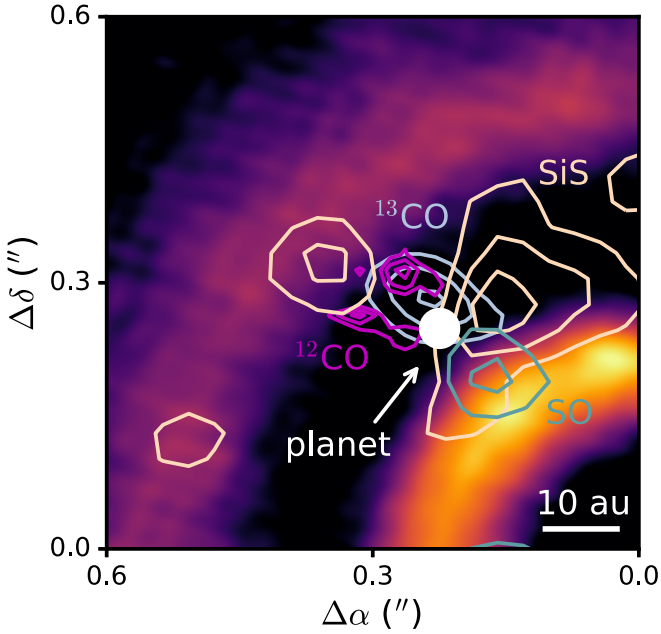

Figure 6. A gallery of chemical signatures related to the HD 169142 b planet. The peak intensities of ^{12}CO (pink), ^{13}CO (blue), SiS (peach), and SO (teal) are shown in contours, and the millimeter dust is in the colorscale. The planet location is indicated by a white circle (Gratton et al. 2019; Hammond et al. 2023). A scale bar showing 10 au is in the lower right corner.

increases to >100 K (Draine et al. 1983), which enables efficient gas-phase formation of SO (e.g., Prasad & Huntress 1980; Hartquist et al. 1980; van Gelder et al. 2021) as well as the thermal desorption of any S-rich ices that are present (e.g., Cleeves et al. 2015; Kama et al. 2019). SO has been detected in only a handful of Class II disks to date, with evidence of gas-phase SO tracing the location of an embedded giant planet in at least one disk (Booth et al. 2023).

SiS. SiS has been detected in a variety of settings in the ISM, including in the circumstellar envelopes of AGB stars (Danilovich et al. 2019; Velilla-Prieto et al. 2019), massive star-forming regions (Tercero et al. 2011), shocks around low-mass protostars (Podio et al. 2017), and the innermost disks of massive protostars (Tanaka et al. 2020; Ginsburg et al. 2023). Unlike the more commonly observed SiO molecule, which is a well-established tracer of silicates released from dust grains in shocks (e.g., Gusdorf et al. 2008), the formation and destruction pathways of SiS remain less clear. While it is possible to produce gas-phase SiS through a direct release from dust cores, this requires strong shocks that fully destroy the grains, and it is inconsistent with existing observations of the low-mass protostellar shock L1157-B1, where SiS is not seen at the jet impact site, i.e., the location of the strongest shocks in this system (Podio et al. 2017). Instead, SiS is thought to be a product of neutral–neutral gas-phase reactions between species released from dust grains in the shock (e.g., Rosi et al. 2018; Paiva et al. 2020). Recent theoretical work has shown a formation route of Si+SH that is efficient at warm temperatures (≈200 K) (Mota et al. 2021), which is consistent with gas temperatures associated with an embedded giant plant. Zanchet et al. (2018) have also suggested a formation route of Si+SO, which may be relevant in HD 169142 given the detection of SO.

The observed chemical signatures of SO and SiS in the HD 169142 disk could thus originate from a variety of mechanisms, including a planet-driven outflow, circumstellar disk winds, planet–disk interactions driving an infall streamer, or emission directly from a circumplanetary disk/envelope.

A planet-driven outflow is the most consistent with the spatial and kinematic properties of both SiS and SO. The SiS has a substantially blueshifted velocity offset (Figure 3) and extends from the planet location along an arc (Figure 1); taken together, these suggest an origin in a localized outflow from an accreting protoplanet. This extended tail is cospatial with the ^{12}CO kinematic excess reported in Garg et al. (2022) (see Appendix E) and is located ahead in azimuth of the (clockwise) planet rotation. This is perhaps somewhat surprising, but we note that the geometry of the emission is not well-constrained and its apparent morphology may be influenced by projection effects. Given the observed blueshift of SiS and nearly face-on orientation of the HD 169142 disk, at least a substantial component of this outflow must be directed along the observer line of sight. Such a geometry is also consistent with an outflow origin of the ^{12}CO and ^{13}CO emission as discussed in Section 5.1.1.

The SO emission is considerably more compact than that of SiS, but it is difficult to tell if this is due to a lack of SO gas or excitation effects. The $J = 19 - 18$ line of SiS has an upper state energy ($E_u = 166$ K) approximately twice that of SO $J = 8_8 - 7_7$ ($E_u = 88$ K). However, with the current coarse velocity resolution and lack of information about SO excitation, we cannot rule out the presence of hot SO gas at or or near the location of the extended SiS emission. The SO emission also does not show the same blueshifted velocity offset as SiS. While this may suggest a non-outflow-based origin such as accretion shocks onto a CPD or a nearby warm gas envelope, it is possible that SO is tracing a different, lower-velocity component of the same outflow.

While there are several alternate explanations for these chemical signatures, they are generally insufficient to simultaneously explain the emission morphology and kinematics of both SiS and SO. Disk winds appear inconsistent with the localized nature of the SO and SiS emission and relatively

small velocity deviations observed (disk winds typically show velocity offsets of tens of km s^{-1} from Keplerian rotation; see, e.g., Booth et al. 2021b). Alternatively, simulations have shown that gap edges become mildly Rayleigh unstable and intermittently shed streams of material into the gap in the presence of high planet masses (Fung & Chiang 2016). However, it is not clear if such wakes result in sufficiently strong shocks to produce detectable amounts of gas-phase SiS. Moreover, detailed analysis of CO kinematics in the HD 169142 disk has found no evidence for such planetary wakes (Garg et al. 2022). While NIR spirals arms are observed in HD 169142, neither SiS nor SO traces the location of these spirals, which are located behind the planet orbit in azimuth (Hammond et al. 2023). It is also unlikely that we are seeing emission from the circumplanetary material itself. The extended morphology of SiS, along with mutual offsets in SO and SiS of a few au from the planet location and CO counterparts (Figure 6), are inconsistent with SO and SiS directly originating from close-in circumplanetary material.

Overall, this suggests that the most plausible scenario is one in which an embedded, giant planet identified in both NIR and via compact ^{12}CO and ^{13}CO emission is driving an outflow, which locally heats gas and produces an extended shock traced in SO and SiS.

5.2. Morphology and Origins of SO Emission

5.2.1. Chemical Origins and Asymmetry

The SO emission distribution in the HD 169142 disk is confined to the innermost ≈70 au and closely follows that of the millimeter dust (Figure 1). The bright asymmetric inner ring is located at the edge of the inner dust cavity, while the faint outer ring appears to peak at the edge of the outer dust ring. This emission distribution is broadly consistent with SO originating from the thermal desorption of S-rich ices (e.g., Cleeves et al. 2011; Kama et al. 2019). This may be due to the direct sublimation of SO ice or gas-phase chemistry following the UV photodissociation of evaporated H_2S and H_2O ices. In the later case, SO can form via the efficient barrierless gas-phase neutral–neutral reactions, S + OH or O + SH (e.g., Charnley 1997). Because both OH and H_2O were not detected with Herschel/PACS (The Photodetector Array Camera and Spectrometer; Fedele et al. 2013) in this disk, this suggests that the ices in HD 169142 are H_2S-rich, although other forms of S-bearing ices cannot be ruled out (e.g., OCS and SO_2).

If the ice reservoir is constrained to the larger mm- and cm-sized dust grains, then the observed asymmetry in SO is difficult to explain with ice sublimation alone, because the dust is largely axisymmetric (Fedele et al. 2017; Macías et al. 2019; Pérez et al. 2019). However, SO asymmetries can be caused by changing physical conditions in the disk, namely azimuthal temperature variations due to a warped disk or dynamical interactions with an embedded planet. We explore each of these scenarios in turn.

Misaligned Inner Disk. Asymmetries in molecular line emission can arise in warped disks from azimuthal variations in disk illumination by the central star, which in turn manifests in chemical variations. Warped disks do not necessarily show clear azimuthal asymmetries in their outer disks, but instead possess misaligned inner disks due to an embedded companion (Young et al. 2021). Models have identified SO as a potential chemical tracer of warped disks and demonstrated that changing X-ray illumination drives variations in SO abundance (Young et al. 2021). The HD 169142 disk shows several signatures of a misaligned inner disk, including shadowing in NIR polarized intensity images (Quanz et al. 2013; Pohl et al. 2017; Bertrang et al. 2018; Rich et al. 2022). On sub-au scales, observations with the GRAVITY instrument at the Very Large Telescope Interferometer revealed a considerable misalignment in both inclination ($i_{in} = 35°$) and position angle ($PA_{in} = 32°$) versus the outer disk ($i = 13°$, $PA = 5°$) as traced by CO (Bohn et al. 2022). Garg et al. (2022) suggested that the kinematic excess observed in ^{12}CO may also originate from a misaligned inner disk, as spurious kinematic residuals can be generated from the subtraction of Keplerian models that incorrectly assume a constant PA and inclination (Young et al. 2022). The HD 169142 disk also shows evidence for a giant planet (≈1–10 M_{Jup}) in its inner dust cavity in observations in the NIR (Bertrang et al. 2020) and of CO isotopologues (Leemker et al. 2022). The models of SO chemical asymmetries in warped disks from Young et al. (2021) were based on a hydrodynamical simulation of a 6.5 M_{Jup} planet embedded in a disk at a radius of 5 au around a solar-mass star orbiting at a 12° inclination with respect to the disk (Nealon et al. 2019). Thus, to first order, this is similar to the HD 169142 system and implies that the presence of a warped disk, due to an embedded giant planet and misaligned inner disk, offers a plausible explanation for the observed SO brightness asymmetry.

Planet–Disk Interactions. It is also possible for dynamical interactions between forming planets and the circumstellar disk to produce chemical asymmetries (e.g., Cleeves et al. 2015). We see evidence of local gas heating at the planet location in the form of compact SO emission (see Section 5.1.2). This additional heating may also contribute, at least in part, to the broader SO asymmetry. The asymmetric, ring-like SO emission likely does not trace accretion shocks but rather the impact of this additional heating on the surrounding disk. It has been shown, for instance, that an embedded giant planet can excite the orbits of planetesimals in the circumstellar gas disk and cause bow-shock heating that evaporates ices (Nagasawa et al. 2019). While the peak of the SO emission brightness is offset in PA from the planet location (Figure 1), we cannot currently discern if this offset has a dynamical origin or is an excitation effect, i.e., we are not observing the hottest SO gas near to the planet location.

5.2.2. Comparison to Other Disks

While SO is commonly observed in protostellar systems (e.g., Bachiller & Pérez Gutiérrez 1997; Codella et al. 2014; Taquet et al. 2020; Garufi et al. 2022), detections are relatively rare in evolved (>1 Myr) Class II protoplanetary disks. HD 169142 is only the fifth such disk where SO has been spatially resolved, after AB Aur (Pacheco-Vázquez et al. 2016; Rivière-Marichalar et al. 2020), Oph-IRS 48 (Booth et al. 2021a), HD 100546 (Booth et al. 2023), and DR Tau (Huang et al. 2023). All of these sources are transition disks around Herbig stars, with the exception of DR Tau, which shows substantial interaction with its environment. There is also a marginal detection of SO in single-dish observations of the transition disk around the T Tauri star GM Aur (Guilloteau et al. 2016), but this disk also shows evidence of late infall from a remnant envelope or cloud material (Huang et al. 2021). Hence, it is not known where the SO is originating from, i.e., disk versus shocks from cloud material. Taken together, this

points to ice sublimation as a common origin for the bulk of SO emission in isolated or noninteracting Class II disks.

The HD 169142 disk appears typical in its SO content relative to other Herbig disks. Its disk-integrated column density is consistent within a factor of a few compared to the HD 100546 ($4.0–6.4 \times 10^{13}$ cm^{-2}; Booth et al. 2023) and AB Aur disks ($2.1–3.4 \times 10^{13}$ cm^{-2}; Rivière-Marichalar et al. 2020). The Oph-IRS 48 disk has a considerably larger SO column density ($4.7–9.9 \times 10^{15}$ cm^{-2}; Booth et al. 2021a), but this disk displays several unique properties, including a high degree of chemical complexity not seen in other Class II disks (van der Marel et al. 2021a; Brunken et al. 2022), which includes the only detection of SO_2 in disks to date (Booth et al. 2021a).

Asymmetries are a common feature of SO emission in protoplanetary disks with all spatially resolved SO observations showing some degree of azimuthal asymmetry. Of those disks with spatially resolved SO, three sources have confirmed (AB Aur b; Currie et al. 2022) or proposed embedded planets (HD 100546 (Currie et al. 2015; Brittain et al. 2019), HD 169142 (Gratton et al. 2019; Hammond et al. 2023)). The AB Aur disk hosts a particularly complex and dynamic environment, with spiral arms and high levels of accretion and outflow activity, and it may be gravitationally unstable (Tang et al. 2012; Salyk et al. 2013; Rivière-Marichalar et al. 2020; Cadman et al. 2021). Thus, disentangling the origin of the SO asymmetry in such a setting is challenging. The HD 100546 disk, however, is a much closer analog to the HD 169412 system, as both are warm Herbig disks with compelling evidence of embedded planets. In both cases, there is a component of SO emission that traces the location of proposed giant planets. In the HD 100546 disk, Booth et al. (2023) also detected temporal variability in the SO emission, which was speculated to be in response to the orbit of an embedded planet. It may be possible to observe similar variability in SO (and possibly SiS) in future observations of the HD 169142 system, although this will require a larger observation baseline, due to the longer rotation period (≈174 yr) associated with a planet at 38 au compared to a 10 au planet in the HD 100546 disk. We do, however, note that these disks are not perfect analogues, as SiS is not detected in HD 100546 and it has a SiS/SO column density ratio of <5.0% (Booth et al. 2023), while this ratio is nearly one-to-one in HD 169412 (Table 2).

6. Conclusions

The HD 169142 disk shows several distinct chemical signatures that demonstrate a compelling link to ongoing giant planet formation. Using ALMA archival data, we identify compact SO $J = 8_8–7_7$ and SiS $J = 19–18$ emission coincident with the position of a proposed $\sim 2\,M_{\rm Jup}$ planet seen as a localized, Keplerian NIR feature within a gas-depleted, annular dust gap at ≈38 au. The SiS emission is non-Keplerian and is located along the same extended azimuthal arc as a known ^{12}CO kinematic excess. This is the first tentative detection of SiS emission in a protoplanetary disk and suggests that the planet is driving sufficiently strong shocks to produce gas-phase SiS. We also report the discovery of compact ^{12}CO $J = 3 - 2$ and ^{13}CO $J = 3 - 2$ emission counterparts coincident with the planet location. Taken together, a planet-driven outflow provides the most consistent explanation for the spatial and kinematic properties of these chemical signatures and their close proximity to the planet position.

In addition to the localized SO emission, we resolve a bright, azimuthally asymmetric SO ring at ≈24 au located at the inner edge of the central dust cavity. This makes HD 169142 only the fifth such Class II system with a spatially resolved SO detection. The bulk of the SO emission likely has an origin in ice sublimation, while its asymmetric distribution suggests the presence of azimuthal temperature variations driven by a misaligned inner disk or planet–disk interactions, possibly due to the giant planet at ≈38 au.

The HD 169142 system presents a powerful template for future searches of planet-related chemical asymmetries in protoplanetary disks and an ideal test bed for observational follow-up. The sudden increase in temperature and density in the shocked gas around the embedded planet likely results in a hot gas-phase chemistry, in which the abundance of several molecular species, in addition to Si- or S-bearing molecules, dramatically increases by several orders of magnitude. Deep spectral surveys of the location around the embedded planet may reveal new chemistry not yet detected in planet-forming disks and allow for new insights into planet-feeding gas. In parallel to this, a survey of SO and SiS emission in disks with known or suspected giant planets would provide a vital confirmation of these molecules as novel tracers of embedded planets.

Acknowledgments

The authors thank the anonymous referee for valuable comments that improved both the content and presentation of this work. We thank Sean Andrews and Richard Teague for useful discussions. This paper makes use of the following ALMA data: ADS/JAO.ALMA#2012.1.00799.S and 2015.1.00806.S. ALMA is a partnership of ESO (representing its member states), NSF (USA) and NINS (Japan), together with NRC (Canada), MOST and ASIAA (Taiwan), and KASI (Republic of Korea), in cooperation with the Republic of Chile. The Joint ALMA Observatory is operated by ESO, AUI/NRAO and NAOJ. The National Radio Astronomy Observatory is a facility of the National Science Foundation operated under cooperative agreement by Associated Universities, Inc. K.I.Ö. acknowledges support from the Simons Foundation (SCOL #686302) and the National Science Foundation under grant No. AST-1907832.

Facility: ALMA.

Software: Astropy (Astropy Collaboration et al. 2013; Price-Whelan et al. 2018), `bettermoments` (Teague & Foreman-Mackey 2018), CASA (McMullin et al. 2007), `cmasher` (van der Velden 2020), `GoFish` (Teague 2019b), `keplerian_mask` (Teague 2020), Matplotlib (Hunter 2007), NumPy (van der Walt et al. 2011), `Photutils` (Bradley et al. 2022).

Appendix A
Observational Details

Table 3 lists all ALMA execution blocks used in this work and includes the ALMA project codes, PIs, UT observing dates, number of antennas, on-source integration times, baseline ranges, observatory-estimated spatial resolutions, maximum recoverable scales (M.R.S.), mean precipitable water vapor (PWV), and flux, phase, and bandpass calibrators.

Table 3
Details of Archival ALMA Observations

Project Code	PI	UT Date	No. Ants.	Int. (min)	Baselines (m)	Res. (″)	M.R.S. (″)	PWV (mm)	Calibrators		
									Flux	Phase	Bandpass
2012.1.00799.S	M. Honda	2015-7-26	41	41.4	15–1574	0.13	1.3	0.4	J1924-2914	J1826-2924	J1924-2914
		2015-7-27	41	21.2	15–1574	0.13	1.4	0.3	J1924-2914	J1826-2924	J1924-2914
		2015-8-8	43	41.4	35–1574	0.13	1.3	1.3	Pallas	J1826-2924	J1924-2914
2015.1.00806.S	J. Pineda	2015-12-6	32	25.3	19–7716	0.031	0.39	1.0	J1733-1304	J1826-2924	J1924-2914

Appendix B
Properties of Compact Emission in SO, ^{12}CO, and ^{13}CO with Various Imaging Parameters

Figure 7 shows SO peak intensity maps for a range of Briggs `robust` values (0.0–2.0). The compact SO emission (NE Blob) is clearly detected in all images. Images with lower `robust` values lack sufficient sensitivity to detect either the NE Blob or the overall ring-like SO structure. Table 4 shows a summary of the properties of the compact SO emission measured from each of these images. We computed the rms, central velocity, FWHM, peak intensity, and integrated intensity within a synthesized beam around the NE Blob. We find that the NE Blob is well detected with peak intensities with S/Ns of ≈5–8. As shown in the last panel of Figure 7, it is also clear that the NE Blob is at a radius distinct from either broad SO ring at 24 au or 50 au and is located near the position of the HD 169142 b planet.

Figure 8 and Table 5 show a similar analysis of the properties of the point-source-like emission in ^{12}CO and ^{13}CO in a range of images with different Briggs `robust` values from 0.0 to 2.0. Images with lower `robust` values lacked sufficient sensitivity to detect the compact ^{12}CO and ^{13}CO emission. For each `robust` value, we also generated images both with and without the JvM correction. Localized emission in the vicinity of HD 169142 b is detected in all image combinations with the exception of the ^{12}CO image at a `robust` of 0.0. However, this image has a considerably higher rms and the smallest beam size so this nondetection is likely due to insufficient sensitivity at these small beam sizes. Depending on the image, the point-source-like ^{12}CO emission was detected with peak S/Ns ranging from ≈3 to 4, while the ^{13}CO emission has peak S/Ns of $\gtrsim$ 3–7. Thus, the detection of ^{12}CO and ^{13}CO emission near HD 169142 b is statistically significant regardless of which image we use.

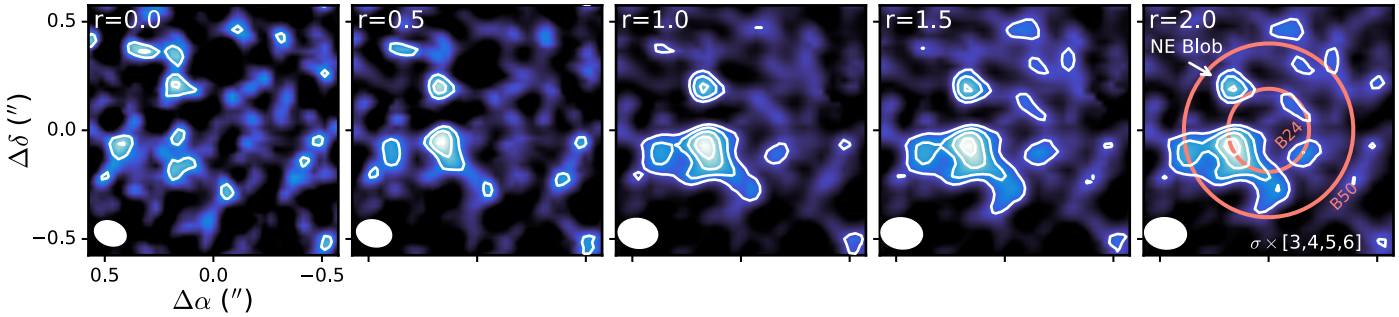

Figure 7. Gallery of SO peak intensity maps generated from images with a range of Briggs `robust` values from 0.0 to 2.0. The location of the NE Blob and the two SO rings are labeled in the rightmost panel. Contours show rms×[3,4,5,6]. The synthesized beam is shown in the lower left corner of each panel.

Table 4
Summary of Compact SO Emission Properties in Various Images

`robust`	Beam (mas × mas)	PA (deg)	rms[a] (mJy beam^{-1})	Central Velocity (km s^{-1})	FWHM (km s^{-1})	Peak Int. (mJy beam^{-1})	Integrated Int. (mJy beam^{-1} km s^{-1})
0.0	150 × 111	69.4	1.41	8.2 ± 0.1	1.9 ± 0.1	7.2 ± 0.7	11.7 ± 1.2
0.5	164 × 123	76.0	1.06	7.9 ± 0.1	1.4 ± 0.1	6.7 ± 0.7	9.6 ± 1.0
1.0	183 × 137	82.2	0.87	7.9 ± 0.1	1.5 ± 0.1	7.0 ± 0.7	9.4 ± 0.9
1.5	192 × 143	84.1	0.88	8.0 ± 0.1	1.5 ± 0.1	6.5 ± 0.6	9.3 ± 0.9
2.0	193 × 144	84.4	0.89	8.0 ± 0.1	1.6 ± 0.1	6.7 ± 0.7	9.8 ± 1.0

Note. We adopt a 10% systematic flux uncertainty and quarter-channel velocity uncertainties.
[a] The rms noise was computed within the synthesized beam around the compact SO emission over the first 20 line-free channels of the cube.

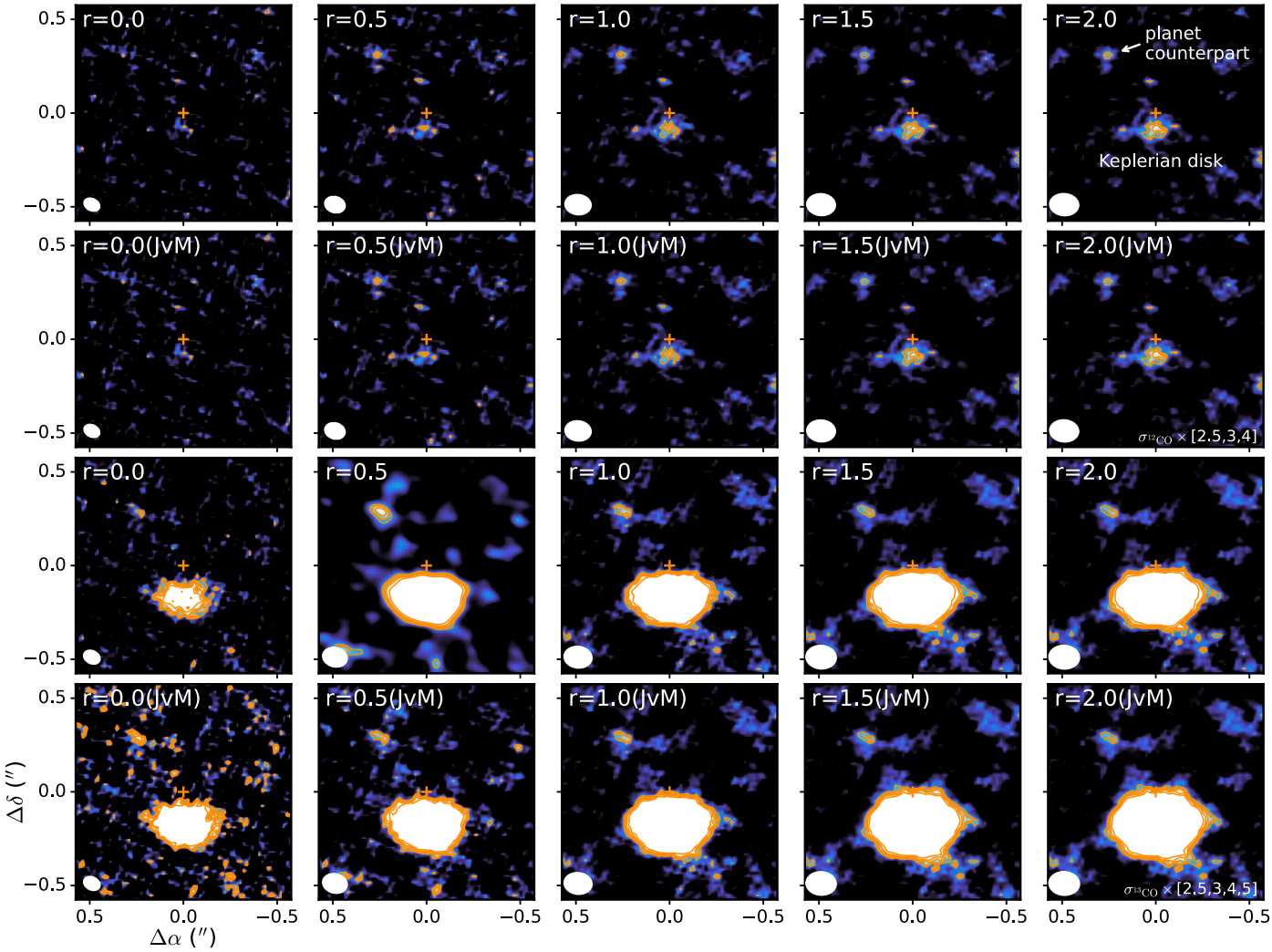

Figure 8. Gallery of selected ^{12}CO and ^{13}CO channels (3.22 and 4.96 km s^{-1}, respectively), which show the peak intensity of the emission counterparts. Images were generated with a range of Briggs `robust` values from 0.0 to 2.0 (left to right) and without (top) and with (bottom) the JvM correction. The locations of the compact emission counterparts and the expected Keplerian rotation are marked in the upper rightmost panel. Contours show rms $\times$[2.5,3,4] and $\times$[2.5,3,4,5] for ^{12}CO and ^{13}CO, respectively. The disk center is marked by a "+" and the synthesized beam is shown in the lower left corner of each panel.

Table 5
Summary of Point-source-like ^{12}CO and ^{13}CO Emission Properties in Various Images

robust	Beam (mas×mas)	PA (deg)	rms[a] (mJy beam^{-1})	Central Velocity (km s^{-1})	FWHM (km s^{-1})	Peak Int. (mJy beam^{-1})	Integrated Int. (mJy beam^{-1} km s^{-1})
^{12}CO $J = 3-2$							
no JvM							
0.0	90 × 66	63.5	3.03	3.33 ± 0.03	0.30 ± 0.03	7.6 ± 0.8	2.0 ± 0.2
0.5	112 × 88	74.1	2.34	3.31 ± 0.03	0.36 ± 0.03	7.1 ± 0.7	2.5 ± 0.2
1.0	142 × 109	83.4	1.51	3.34 ± 0.03	0.43 ± 0.03	5.6 ± 0.6	1.7 ± 0.2
1.5	155 × 118	86.1	1.21	3.36 ± 0.03	0.48 ± 0.03	4.5 ± 0.4	1.4 ± 0.1
2.0	157 × 119	85.6	1.18	3.36 ± 0.03	0.48 ± 0.03	4.4 ± 0.4	1.4 ± 0.1
^{12}CO $J = 3-2$							
with JvM							
0.0	90 × 66	63.5	1.71	3.33 ± 0.03	0.30 ± 0.03	4.3 ± 0.4	1.1 ± 0.1
0.5	112 × 87	74.1	1.49	3.31 ± 0.03	0.36 ± 0.03	4.5 ± 0.5	1.6 ± 0.2
1.0	142 × 109	83.4	0.87	3.34 ± 0.03	0.43 ± 0.03	3.3 ± 0.3	1.0 ± 0.1
1.5	154 × 118	86.1	0.62	3.36 ± 0.03	0.48 ± 0.03	2.3 ± 0.2	0.7 ± 0.1
2.0	157 × 119	85.6	0.60	3.36 ± 0.03	0.48 ± 0.03	2.2 ± 0.2	0.7 ± 0.1
^{13}CO $J = 3-2$							
no JvM							
0.0	94 × 71	63.4	1.89	5.04 ± 0.03	0.54 ± 0.03	11.6 ± 1.2	5.8 ± 0.6
0.5	135 × 105	76.3	1.45	5.01 ± 0.03	0.51 ± 0.03	8.7 ± 0.9	3.9 ± 0.4
1.0	151 × 117	83.5	1.46	5.01 ± 0.03	0.44 ± 0.03	6.1 ± 0.6	2.6 ± 0.3
1.5	163 × 127	86.0	1.59	5.00 ± 0.03	0.41 ± 0.03	5.4 ± 0.5	2.2 ± 0.2
2.0	165 × 128	86.5	1.62	5.00 ± 0.03	0.42 ± 0.03	5.4 ± 0.5	2.2 ± 0.2
^{13}CO $J = 3-2$							
with JvM							
0.0	94 × 71	63.4	1.08	5.04 ± 0.03	0.54 ± 0.03	6.6 ± 0.7	3.3 ± 0.3
0.5	135 × 105	76.3	0.88	5.01 ± 0.03	0.51 ± 0.03	6.0 ± 0.6	2.7 ± 0.3
1.0	151 × 117	83.5	0.85	5.01 ± 0.03	0.44 ± 0.03	3.6 ± 0.4	1.5 ± 0.2
1.5	163 × 127	86.0	0.85	5.00 ± 0.03	0.41 ± 0.03	2.9 ± 0.3	1.2 ± 0.1
2.0	165 × 128	86.5	0.85	5.00 ± 0.03	0.42 ± 0.03	2.8 ± 0.3	1.2 ± 0.1

Note. We adopt a 10% systematic flux uncertainty and quarter-channel velocity uncertainties.
[a] The rms noise was computed within the synthesized beam around the compact ^{12}CO and ^{13}CO emission over the first 20 line-free channels of the cube.

Appendix C
Channel Maps

Channel maps of SO $J = 8_8 - 7_7$ and SiS $J = 19 - 18$ are shown in Figures 9 and 10, respectively.

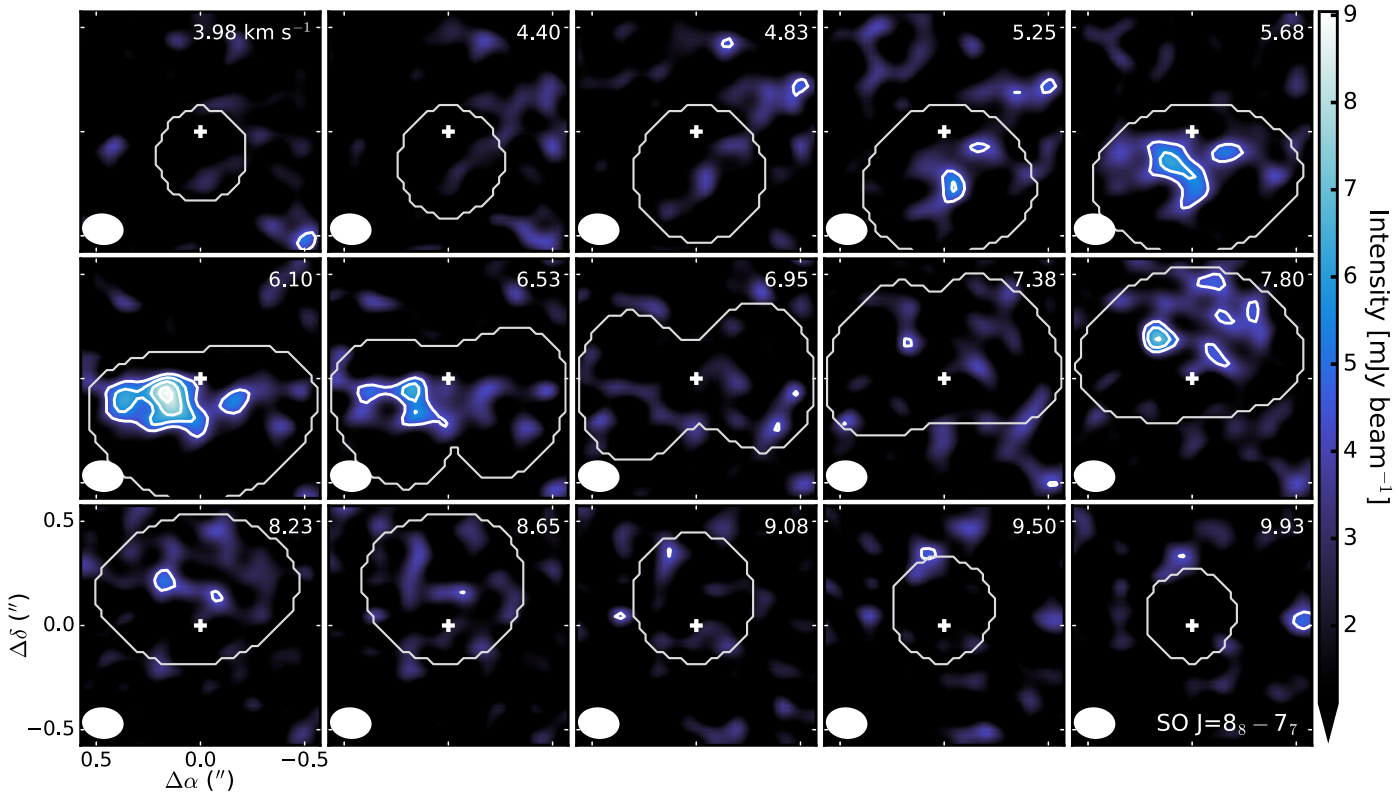

Figure 9. Channel maps of the SO $J = 8_8$–7_7 emission of the HD 169142 disk. A representative Keplerian mask is shown in light gray. Contours show rms×[3,4,5,6]. The synthesized beam is shown in the lower left corner of each panel, and the LSRK velocity in km s^{-1} is printed in the upper right.

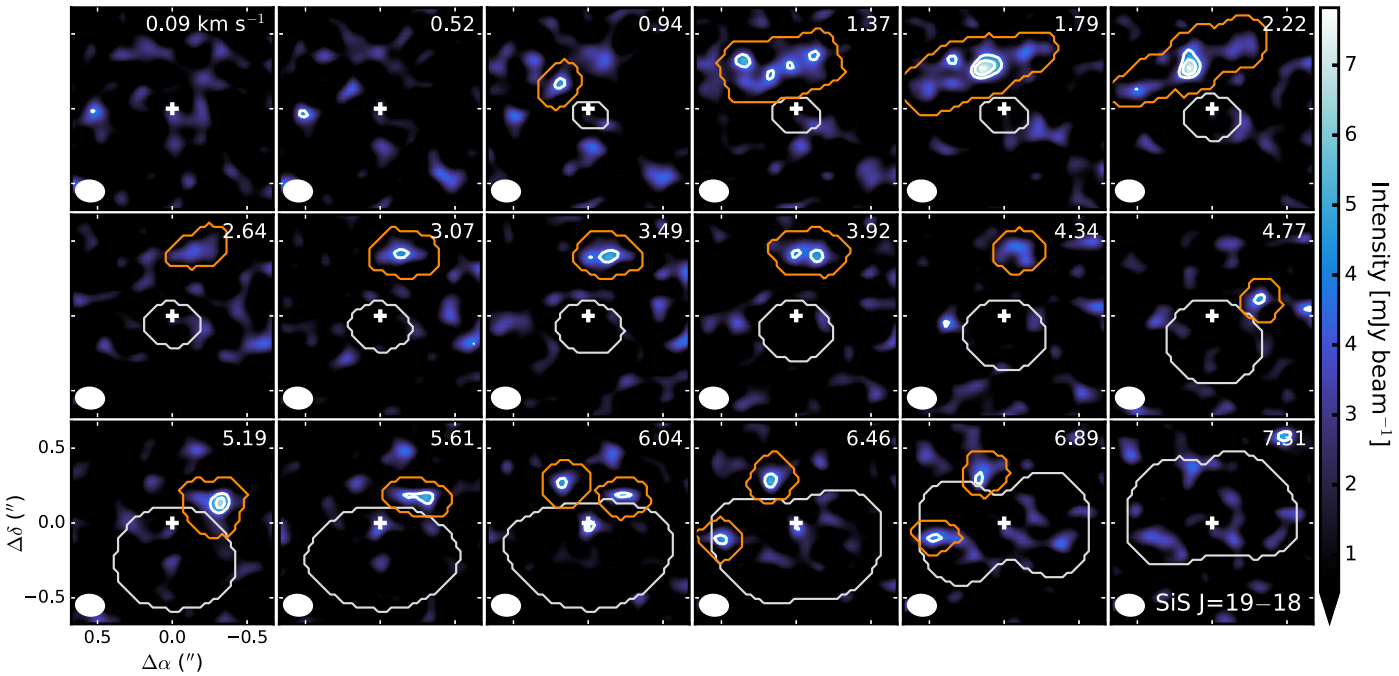

Figure 10. Channel maps of the SiS $J = 19$−18 emission of the HD 169142 disk. Contours show rms×[3,4,5]. The hand-drawn masks are marked in orange. Otherwise, as in Figure 9.

Appendix D
Centroid Measurements of Compact ^{12}CO and ^{13}CO Emission

We computed the centroid of the point-source-like emission in ^{12}CO and ^{13}CO $J = 3 - 2$ on a per-channel basis. We used the `centroid_2dg` task in `Photutils` (Bradley et al. 2022) Python package to fit a 2D Gaussian to the emission distribution. Table 6 reports the derived centroids and Figure 11 shows their positions.

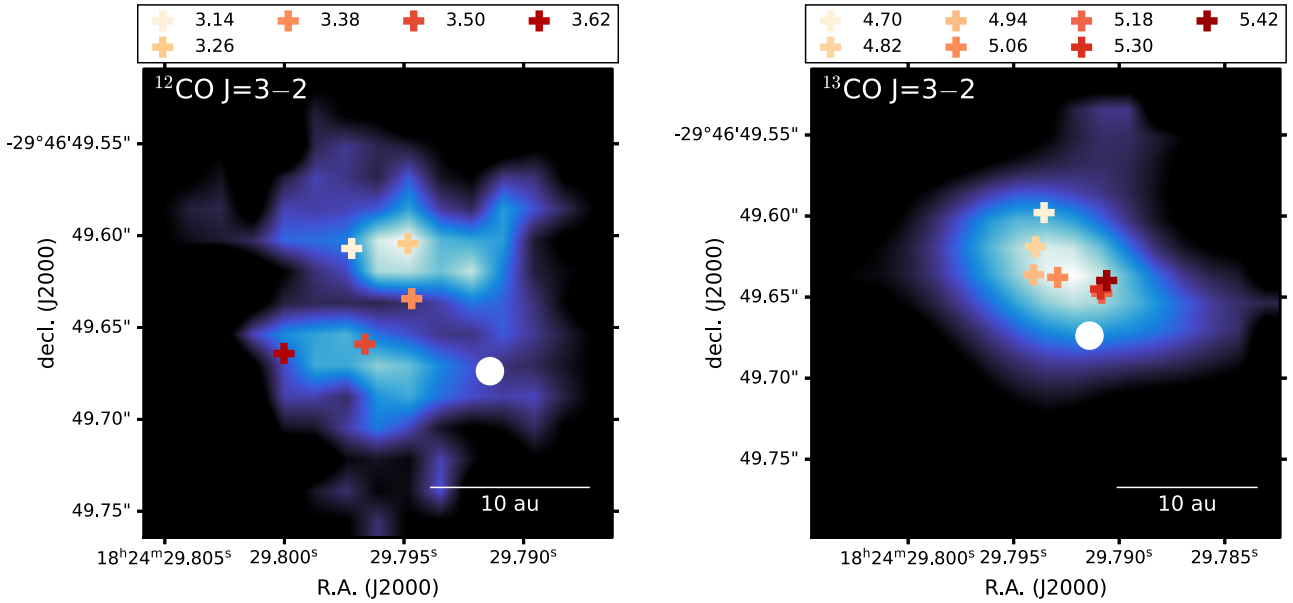

Figure 11. Centroid measurements for the compact ^{12}CO and ^{13}CO emission over the velocity range in which it is detected. Colors indicate the LSRK velocity in km s^{-1} at which the centroid was derived. The location of the HD 169142 b planet is shown by a white circle (Gratton et al. 2019; Hammond et al. 2023). A scale bar showing 10 au is in the lower right.

Table 6
Centroid Positions of Compact ^{12}CO and ^{13}CO Emission

Velocity (km s^{-1})	R.A. (J2000)	decl. (J2000)	R.A. Offset (″)	decl. Offset (″)
^{12}CO $J = 3 - 2$				
3.14	$18^h24^m29\overset{s}{.}7972$	$-29^d46^m49\overset{s}{.}6070$	0.303	0.319
3.26	$18^h24^m29\overset{s}{.}7948$	$-29^d46^m49\overset{s}{.}6043$	0.272	0.322
3.38	$18^h24^m29\overset{s}{.}7947$	$-29^d46^m49\overset{s}{.}6343$	0.271	0.292
3.50	$18^h24^m29\overset{s}{.}7966$	$-29^d46^m49\overset{s}{.}6590$	0.296	0.267
3.62	$18^h24^m29\overset{s}{.}8000$	$-29^d46^m49\overset{s}{.}6642$	0.340	0.262
^{13}CO $J = 3 - 2$				
4.70	$18^h24^m29\overset{s}{.}7936$	$-29^d46^m49\overset{s}{.}5979$	0.256	0.328
4.82	$18^h24^m29\overset{s}{.}7940$	$-29^d46^m49\overset{s}{.}6190$	0.261	0.307
4.94	$18^h24^m29\overset{s}{.}7941$	$-29^d46^m49\overset{s}{.}6362$	0.262	0.290
5.06	$18^h24^m29\overset{s}{.}7929$	$-29^d46^m49\overset{s}{.}6379$	0.248	0.288
5.18	$18^h24^m29\overset{s}{.}7908$	$-29^d46^m49\overset{s}{.}6477$	0.220	0.278
5.30	$18^h24^m29\overset{s}{.}7909$	$-29^d46^m49\overset{s}{.}6451$	0.221	0.281
5.42	$18^h24^m29\overset{s}{.}7906$	$-29^d46^m49\overset{s}{.}6398$	0.217	0.286

Note. Offset positions are computed from the phase center of the observations ($\alpha = 18^h24^m29\overset{s}{.}774$, $\delta = -29^d46^m49\overset{s}{.}926$).

Appendix E
SiS Emission versus CO Kinematic Excess

Figure 12 shows the ^{12}CO $J = 2 - 1$ kinematic excess reported in Garg et al. (2022) with the integrated intensity of SiS $J = 19 - 18$ overlaid. The SiS emission is cospatial with the azimuthal arc of the ^{12}CO kinematic excess.

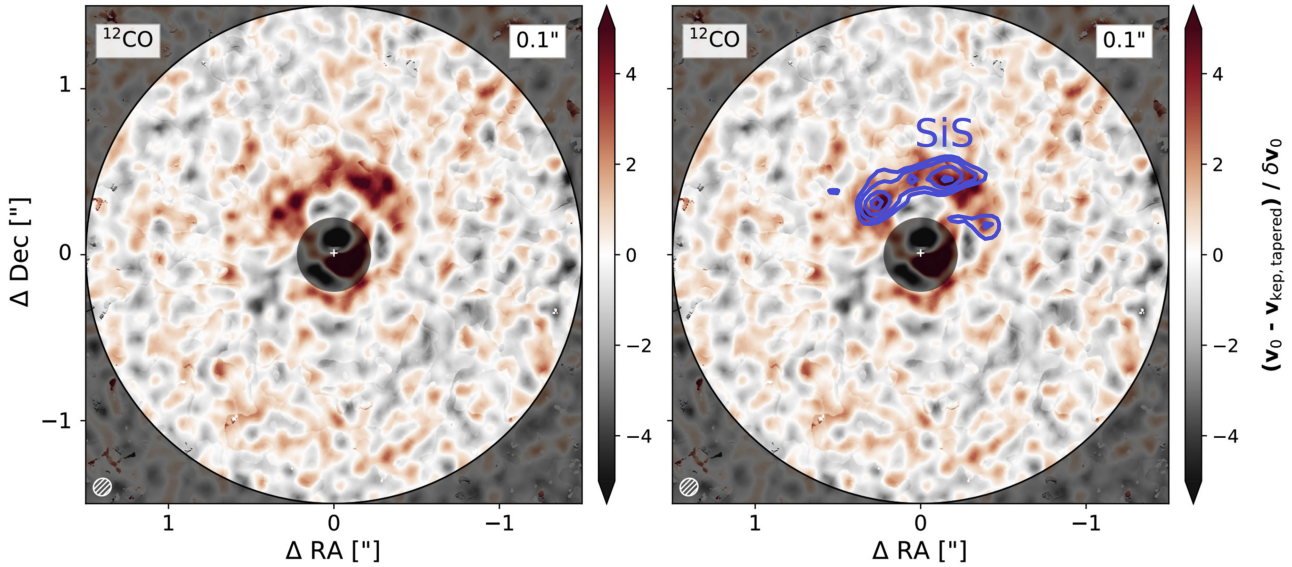

Figure 12. ^{12}CO $J = 2 - 1$ kinematic excess (left) and with the zeroth-moment map of SiS overlaid in contours (right). Background figure reproduced from Garg et al. (2022).

ORCID iDs

Charles J. Law https://orcid.org/0000-0003-1413-1776
Alice S. Booth https://orcid.org/0000-0003-2014-2121
Karin I. Öberg https://orcid.org/0000-0001-8798-1347

References

Alarcón, F., Bergin, E. A., & Teague, R. 2022, ApJL, 941, L24
ALMA Partnership, Brogan, C. L., Pérez, L. M, et al. 2015, ApJL, 808, L3
Andrews, S. M., Elder, W., Zhang, S., et al. 2021, ApJ, 916, 51
Andrews, S. M., Huang, J., Pérez, L. M., et al. 2018, ApJL, 869, L41
Astropy Collaboration, Robitaille, T. P., Tollerud, E. J., et al. 2013, A&A, 558, A33
Bachiller, R., & Pérez Gutiérrez, M. 1997, ApJL, 487, L93
Bae, J., Teague, R., Andrews, S. M., et al. 2022, ApJL, 934, L20
Bailer-Jones, C. A. L., Rybizki, J., Fouesneau, M., Demleitner, M., & Andrae, R. 2021, AJ, 161, 147
Benisty, M., Bae, J., Facchini, S., et al. 2021, ApJL, 916, L2
Bergner, J. B., Öberg, K. I., Bergin, E. A., et al. 2019, ApJ, 876, 25
Bertrang, G. H. M., Avenhaus, H., Casassus, S., et al. 2018, MNRAS, 474, 5105
Bertrang, G. H. M., Flock, M., Keppler, M., et al. 2020, arXiv:2007.11565
Blondel, P. F. C., & Djie, H. R. E. T. A. 2006, A&A, 456, 1045
Bohn, A. J., Benisty, M., Perraut, K., et al. 2022, A&A, 658, A183
Booth, A. S., Ilee, J. D., Walsh, C., et al. 2023, A&A, 669, A53
Booth, A. S., Tabone, B., Ilee, J. D., et al. 2021b, ApJS, 257, 16
Booth, A. S., van der Marel, N., Leemker, M., van Dishoeck, E. F., & Ohashi, S. 2021a, A&A, 651, L6
Booth, A. S., Walsh, C., Kama, M., et al. 2018, A&A, 611, A16
Bradley, L., Sipőcz, B., Robitaille, T., et al. 2022, astropy/photutils: v1.5.0, Zenodo, doi:10.5281/zenodo.6825092
Brittain, S. D., Najita, J. R., & Carr, J. S. 2019, ApJ, 883, 37
Brunken, N. G. C., Booth, A. S., Leemker, M., et al. 2022, A&A, 659, A29
Cadman, J., Rice, K., & Hall, C. 2021, MNRAS, 504, 2877
Charnley, S. B. 1997, ApJ, 481, 396
Cieza, L. A., González-Ruilova, C., Hales, A. S., et al. 2021, MNRAS, 501, 2934
Cleeves, L. I., Bergin, E. A., Bethell, T. J., et al. 2011, ApJL, 743, L2
Cleeves, L. I., Bergin, E. A., & Harries, T. J. 2015, ApJ, 807, 2
Codella, C., Maury, A. J., Gueth, F., et al. 2014, A&A, 563, L3
Currie, T., Cloutier, R., Brittain, S., et al. 2015, ApJL, 814, L27
Currie, T., Lawson, K., Schneider, G., et al. 2022, NatAs, 6, 751
Czekala, I., Loomis, R. A., Teague, R., et al. 2021, ApJS, 257, 2
Danilovich, T., Richards, A. M. S., Karakas, A. I., et al. 2019, MNRAS, 484, 494
Draine, B. T., Roberge, W. G., & Dalgarno, A. 1983, ApJ, 264, 485
Endres, C. P., Schlemmer, S., Schilke, P., Stutzki, J., & Müller, H. S. P. 2016, JMoSp, 327, 95
Facchini, S., Teague, R., Bae, J., et al. 2021, AJ, 162, 99
Fedele, D., Bruderer, S., van Dishoeck, E. F., et al. 2013, A&A, 559, A77
Fedele, D., Carney, M., Hogerheijde, M. R., et al. 2017, A&A, 600, A72
Fung, J., & Chiang, E. 2016, ApJ, 832, 105
Gaia Collaboration, Brown, A. G. A., Vallenari, A., et al. 2021, A&A, 649, A1
Garg, H., Pinte, C., Hammond, I., et al. 2022, MNRAS, 517, 5942
Garufi, A., Podio, L., Codella, C., et al. 2022, A&A, 658, A104
Ginsburg, A., McGuire, B. A., Sanhueza, P., et al. 2023, ApJ, 942, 66
Gratton, R., Ligi, R., Sissa, E., et al. 2019, A&A, 623, A140
Guilloteau, S., Reboussin, L., Dutrey, A., et al. 2016, A&A, 592, A124
Gusdorf, A., Pineau Des Forêts, G., Cabrit, S., & Flower, D. R. 2008, A&A, 490, 695
Hammond, I., Christiaens, V., Price, D. J., et al. 2023, MNRAS, 522, L51
Harsono, D., van der Wiel, M. H. D., Bjerkeli, P., et al. 2021, A&A, 646, A72
Hartquist, T. W., Dalgarno, A., & Oppenheimer, M. 1980, ApJ, 236, 182
Honda, M., Maaskant, K., Okamoto, Y. K., et al. 2012, ApJ, 752, 143
Huang, J., Andrews, S. M., Dullemond, C. P., et al. 2018, ApJL, 869, L42
Huang, J., Bergin, E. A., Bae, J., Benisty, M., & Andrews, S. M. 2023, ApJ, 943, 107
Huang, J., Bergin, E. A., Öberg, K. I., et al. 2021, ApJS, 257, 19
Hunter, J. D. 2007, CSE, 9, 90
Isella, A., Chandler, C. J., Carpenter, J. M., Pérez, L. M., & Ricci, L. 2014, ApJ, 788, 129
Jorsater, S., & van Moorsel, G. A. 1995, AJ, 110, 2037
Kama, M., Shorttle, O., Jermyn, A. S., et al. 2019, ApJ, 885, 114
Kanagawa, K. D., Muto, T., Tanaka, H., et al. 2015, ApJL, 806, L15
Karlin, S. M., Panić, O., & van Loo, S. 2023, MNRAS, 520, 1258
Keppler, M., Benisty, M., Müller, A., et al. 2018, A&A, 617, A44
Law, C. J., Loomis, R. A., Teague, R., et al. 2021, ApJS, 257, 3
Lee, C.-F., Li, Z.-Y., Codella, C., et al. 2018, ApJ, 856, 14
Leemker, M., Booth, A. S., van Dishoeck, E. F., et al. 2022, A&A, 663, A23
Ligi, R., Vigan, A., Gratton, R., et al. 2018, MNRAS, 473, 1774
Macías, E., Espaillat, C. C., Osorio, M., et al. 2019, ApJ, 881, 159
McMullin, J. P., Waters, B., Schiebel, D., Young, W., & Golap, K. 2007, in ASP Conf. Ser. 376, Astronomical Data Analysis Software and Systems XVI, ed. R. A. Shaw, F. Hill, & D. J. Bell (San Francisco, CA: ASP), 127
Mota, V. C., Varandas, A. J. C., Mendoza, E., Wakelam, V., & Galvão, B. R. L. 2021, ApJ, 920, 37
Müller, H. S. P., Schlöder, F., Stutzki, J., & Winnewisser, G. 2005, JMoSt, 742, 215
Müller, H. S. P., Thorwirth, S., Roth, D. A., & Winnewisser, G. 2001, A&A, 370, L49
Nagasawa, M., Tanaka, K. K., Tanaka, H., et al. 2019, ApJ, 871, 110
Nealon, R., Pinte, C., Alexander, R., Mentiplay, D., & Dipierro, G. 2019, MNRAS, 484, 4951
Öberg, K. I., Guzmán, V. V., Walsh, C., et al. 2021, ApJS, 257, 1
Osorio, M., Anglada, G., Carrasco-González, C., et al. 2014, ApJL, 791, L36
Oya, Y., López-Sepulcre, A., Sakai, N., et al. 2019, ApJ, 881, 112
Pacheco-Vázquez, S., Fuente, A., Baruteau, C., et al. 2016, A&A, 589, A60
Paiva, M. A. M., Lefloch, B., & Galvão, B. R. L. 2020, MNRAS, 493, 299
Panić, O., Hogerheijde, M. R., Wilner, D., & Qi, C. 2008, A&A, 491, 219
Pérez, S., Casassus, S., Baruteau, C., et al. 2019, AJ, 158, 15
Perez, S., Dunhill, A., Casassus, S., et al. 2015, ApJL, 811, L5
Pineda, J. E., Szulágyi, J., Quanz, S. P., et al. 2019, ApJ, 871, 48
Pinte, C., Hammond, I., Price, D. J., et al. 2023, MNRAS, Advance Access
Pinte, C., Price, D. J., Ménard, F., et al. 2020, ApJL, 890, L9
Podio, L., Codella, C., Lefloch, B., et al. 2017, MNRAS, 470, L16
Pohl, A., Benisty, M., Pinilla, P., et al. 2017, ApJ, 850, 52
Prasad, S. S., & Huntress, W. T. J. 1980, ApJS, 43, 1
Price-Whelan, A. M., Sipőcz, B. M., Günther, H. M., et al. 2018, AJ, 156, 123
Quanz, S. P., Avenhaus, H., Buenzli, E., et al. 2013, ApJL, 766, L2
Rab, C., Kamp, I., Ginski, C., et al. 2019, A&A, 624, A16
Raman, A., Lisanti, M., Wilner, D. J., Qi, C., & Hogerheijde, M. 2006, AJ, 131, 2290
Reggiani, M., Quanz, S. P., Meyer, M. R., et al. 2014, ApJL, 792, L23
Rice, W. K. M., Armitage, P. J., Wood, K., & Lodato, G. 2006, MNRAS, 373, 1619
Rich, E. A., Monnier, J. D., Aarnio, A., et al. 2022, AJ, 164, 109
Rivière-Marichalar, P., Fuente, A., Le Gal, R., et al. 2020, A&A, 642, A32
Rosi, M., Mancini, L., Skouteris, D., et al. 2018, CPL, 695, 87
Sakai, N., Oya, Y., Higuchi, A. E., et al. 2017, MNRAS, 467, L76
Sakai, N., Sakai, T., Hirota, T., et al. 2014, Natur, 507, 78
Salyk, C., Herczeg, G. J., Brown, J. M., et al. 2013, ApJ, 769, 21
Szulágyi, J. 2017, ApJ, 842, 103
Szulágyi, J., Plas, G. V. D., Meyer, M. R, et al. 2018, MNRAS, 473, 3573
Tabone, B., Cabrit, S., Bianchi, E., et al. 2017, A&A, 607, L6
Tanaka, K. E. I., Zhang, Y., Hirota, T., et al. 2020, ApJL, 900, L2
Tang, Y. W., Guilloteau, S., Piétu, V., et al. 2012, A&A, 547, A84
Taquet, V., Codella, C., De Simone, M., et al. 2020, A&A, 637, A63
Teague, R. 2019a, RNAAS, 3, 74
Teague, R. 2019b, JOSS, 4, 1632
Teague, R. 2020, richteague/keplerian_mask: Initial Release, v1.0, Zenodo, doi:10.5281/zenodo.4321137
Teague, R., Bae, J., Bergin, E. A., Birnstiel, T., & Foreman-Mackey, D. 2018, ApJL, 860, L12
Teague, R., & Foreman-Mackey, D. 2018, Bettermoments: A Robust Method To Measure Line Centroids, v1.0, Zenodo, doi:10.5281/zenodo.1419754
Tercero, B., Vincent, L., Cernicharo, J., Viti, S., & Marcelino, N. 2011, A&A, 528, A26
Toci, C., Lodato, G., Fedele, D., Testi, L., & Pinte, C. 2020, ApJL, 888, L4
van der Marel, N., Birnstiel, T., Garufi, A., et al. 2021b, AJ, 161, 33
van der Marel, N., Booth, A. S., Leemker, M., van Dishoeck, E. F., & Ohashi, S. 2021a, A&A, 651, L5
van der Velden, E. 2020, JOSS, 5, 2004
van der Walt, S., Colbert, S. C., & Varoquaux, G. 2011, CSE, 13, 22
van Gelder, M. L., Tabone, B., van Dishoeck, E. F., & Godard, B. 2021, A&A,

653, A159
van Terwisga, S. E., van Dishoeck, E. F., Cazzoletti, P., et al. 2019, A&A, 623, A150
Velilla-Prieto, L., Cernicharo, J., Agúndez, M., et al. 2019, A&A, 629, A146
Wu, Y.-L., Bowler, B. P., Sheehan, P. D., et al. 2022, ApJL, 930, L3
Young, A. K., Alexander, R., Rosotti, G., & Pinte, C. 2022, MNRAS, 513, 487
Young, A. K., Alexander, R., Walsh, C., et al. 2021, MNRAS, 505, 4821
Yu, H., Teague, R., Bae, J., & Öberg, K. 2021, ApJL, 920, L33
Zanchet, A., Roncero, O., Agúndez, M., & Cernicharo, J. 2018, ApJ, 862, 38
Zhang, S., Zhu, Z., Huang, J., et al. 2018, ApJL, 869, L47